Solving 2D and 3D Lattice Models of Correlated Fermions—Combining Matrix Product States with Mean-Field Theory

Gunnar Bollmark,[1,*] Thomas Köhler,[1] Lorenzo Pizzino,[2] Yiqi Yang,[3] Johannes S. Hofmann,[4] Hao Shi,[5]
Shiwei Zhang,[6] Thierry Giamarchi,[2] and Adrian Kantian[1,7,†]

[1]*Department of Physics and Astronomy, Uppsala University, Box 516, S-751 20, Uppsala, Sweden*
[2]*DQMP, University of Geneva, 24 Quai Ernest-Ansermet, 1211 Geneva, Switzerland*
[3]*Department of Physics, College of William and Mary, Williamsburg, Virginia 23187, USA*
[4]*Department of Condensed Matter Physics, Weizmann Institute of Science, Rehovot 76100, Israel*
[5]*Department of Physics and Astronomy, University of Delaware, Newark, Delaware 19716, USA*
[6]*Center for Computational Quantum Physics, Flatiron Institute,
162 Fifth Avenue, New York, New York, 10010, USA*
[7]*SUPA, Institute of Photonics and Quantum Sciences, Heriot-Watt University,
Edinburgh EH14 4AS, United Kingdom*

Correlated electron states are at the root of many important phenomena including unconventional superconductivity (USC), where electron pairing arises from repulsive interactions. Computing the properties of correlated electrons, such as the critical temperature T_c for the onset of USC, efficiently and reliably from the microscopic physics with quantitative methods remains a major challenge for almost all models and materials. In this theoretical work, we combine matrix product states (MPS) with static mean field (MF) to provide a solution to this challenge for quasi-one-dimensional (Q1D) systems: two- and three-dimensional materials comprised of weakly coupled correlated 1D fermions. This MPS + MF framework for the ground state and thermal equilibrium properties of Q1D fermions is developed and validated for attractive Hubbard systems first, and further enhanced via analytical field theory. We then deploy it to compute T_c for superconductivity in 3D arrays of weakly coupled, doped, and repulsive Hubbard ladders. The MPS + MF framework thus enables the quantitative study of USC and high-T_c superconductivity—and potentially many more correlated phases—in fermionic Q1D systems based directly on their microscopic parameters, in ways inaccessible to previous methods. This approach further allows one to treat competing macroscopic orders, such as superconducting and insulating ones, on an equal footing. Benchmarks of the framework using auxiliary-field quantum Monte Carlo techniques show that the overestimation of, e.g., T_c due to its mean-field component, is near constant in microscopic parameters. These features of the MPS + MF approach to correlated fermions open up the possibility of designing deliberately optimized Q1D superconductors, from experiments in ultracold gases to synthesizing new materials.

I. INTRODUCTION

Obtaining quantitative and reliable solutions to strongly-correlated-fermion models from first principles is one of the greatest challenges to the theory of quantum matter, arising in many different areas, from solid-state physics to ultracold atomic gases. Its prominence derives, to a large degree, from the fundamental and technological importance of many of the collective quantum states emerging from electronic correlations.

Unconventional superconductivity (USC) epitomizes this challenge: Repulsive interactions lead to electrons forming correlated pairs which attain macroscopic phase coherence and enter a superconducting state at the critical temperature T_c. Crucially, the high-T_c superconducting models and materials belong to this group [1–3]. These can be divided into two classes: the quasi-two-dimensional (Q2D) models and materials, and the quasi-one-dimensional (Q1D) ones. In both cases, the relevant three-dimensional (3D) system is comprised of weakly

coupled lower-dimensional subunits, 2D and 1D ones for Q2D and Q1D, respectively.

The present work introduces a quantitative and efficient theoretical framework for Q1D systems capable of calculating properties of unconventional and high-T_c superconductivity from microscopic parameters, as well treating its competition with other correlated phases of fermions. As the overestimation of, e.g., T_c that is inherent in the mean-field component of the framework is by a constant factor, this framework allows us to deliberately engineer high-T_c superconductivity from the bottom up in such systems.

This is achieved by leveraging two unique advantages with respect to USC that the 1D subunits within a Q1D system can have compared to the known 2D subunits in the Q2D ones: (1) The microscopic mechanism of pair formation from repulsive interactions can typically be worked out [4]. (2) The pairing energy resulting from it can be computed accurately from microscopic parameters [5,6]. These pairing energies can moreover be very high. For doped two-leg Hubbard ladders, pairing energies up to about 15% of electron tunneling have already been demonstrated [5], as the 1D nature of these ladders naturally enhances the repulsively mediated effective attraction. As fluctuations preclude superconductivity in isolated 1D subunits, the coupling of these ladders into a three-dimensional Q1D array is essential to enable macroscopic ordering of pair phases.

Analysis of the resulting arrays has so far been limited to Tomonaga-Luttinger-liquid (TLL) field theory [4] combined with static mean-field (MF) techniques [5,7]. The TLL approach has many uses, such as explaining repulsively mediated pairing, or mapping the low-energy theory of Hubbard ladders to that of the simpler negative-U Hubbard chains. However, it allows neither the computation of T_c of a Q1D array quantitatively nor the determination of whether it realizes USC or another correlated phase from microscopic parameters. Furthermore, this approach also disregards exchange processes between 1D subunits. Thus, it cannot inform the search for USC

and high-T_c systems in the Q1D space, be it for synthesizing candidate materials or guiding quantum simulations toward analog states of USC within current experimental capabilities. Both are intensely sought goals that remain highly challenging for the theory of Q2D superconductors with repulsively mediated pairing [1,2,8–14]. The latter issue is acute for finding USC-like states in highly controlled ultracold-gas experiments with fermions, i.e., analog quantum simulators, for the 2D Hubbard models [15–20]. As current theory cannot efficiently determine where and whether these experimental setups realize a USC state within the achievable entropies, the impasse on classical computational theory for 2D fermions still impedes progress on the quantum simulation front.

Shifting focus to Q1D systems instead, this work establishes a numerical theory framework capable of meeting these aims. We further enhance the framework via novel TLL + MF theory that allows us to compute T_c from easier-to-obtain zero-temperature numerics. Briefly summarized, the framework exploits that in the weak-coupling regime between the 1D subunits, we can apply perturbation theory in the ratio of the single-fermion tunneling in between 1D subunits to the pairing energy. We show how this ratio naturally controls the possible superconducting T_c. In this perturbative regime, which is different from USC and high-T_c superconductivity in Q2D system such as the cuprates, the full 3D array can be decoupled via static MF theory. This treatment maps the problem to that of a single 1D subunit with multiple MF amplitudes, which is then solved self-consistently at the microscopic level. As summarized in Fig. 1, these represent the various possible injections or ejections of fermion pairs into or out of the 1D subunit stemming from the 3D array, as well as the previously neglected exchange processes. Single-fermion tunneling in between 1D subunits is naturally suppressed in this perturbative regime. While this reliance on a gap within the 1D subunits might appear limiting, it is a key advantage over USC systems based on Q2D subunits without such a
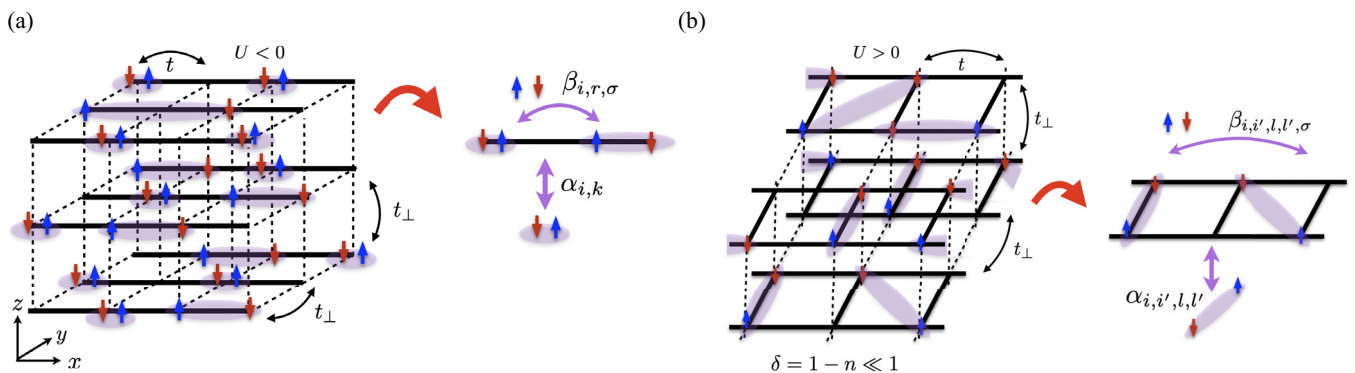

FIG. 1. Overview of MPS + MF for fermions. A 3D array composed of weakly coupled 1D subunits is mapped onto a self-consistent 1D problem with mean-field amplitudes $\alpha_{i,k}$ and $\beta_{i,r,\sigma}$. (a) Array of negative-U Hubbard chains, with on-site attraction U, tunneling t along the chain, and interchain tunneling $t_\perp$. (b) Array of repulsive-U-doped Hubbard ladders. Doping levels are δ, n.n. tunneling (nearest-neighbor tunneling) inside the ladders is t and $t_\perp$ in between them.

gap, as it breaks the task of understanding and optimizing USC overall down into two separate, much better controlled ones: how electrons pair within the 1D subunit, which is already solved for many systems and where pairing can be cheaply optimized for isolated 1D subunits, and how the pairs then attain macroscopic phase coherence, which is the main focus of the present work.

This framework is not limited to superconductivity. It can be applied to any fermionic Q1D setup in which the 1D subunits have some type of gap sufficient for intersystem tunneling to be relevant first at second order. Such a regime is realized, for instance, in the various insulating phases of the Bechgaard and Fabre salts [21,22]. Alternatively, such regimes may be found, with minor modifications, in the recently proposed and partially realized mixed-dimensional large-J systems in ultracold fermionic lattice gases [23,24]. At the same time, the quantitative study of USC regimes of the same compounds, as well as of other Q1D materials such as chromium pnictide [25,26] and the telephone-number compounds [27,28], would require including single-electron tunneling in between 1D subunits. This would be beyond the MPS + MF framework described here, necessitating an approach akin to chain dynamical mean-field theory (chain DMFT) [29,30]. For many Q1D systems of acute interest for designing novel high-T_c superconductors, such as arrays of doped repulsive-U Hubbard ladders, this approach would, however, necessitate redeveloping chain DMFT with a MPS-based solver such as to avoid the sign problem of quantum Monte Carlo (QMC)-based solvers [31]. At present, for systems of relevant size, we however envision the bipartite entanglement to be prohibitively large.

The present work hinges on an efficient, reliable numerical method at the microscopic level for correlated-fermion 1D subunits including MF amplitudes. Algorithms using matrix product states (MPS) [32], such as the density matrix renormalization group (DMRG) [33,34] are uniquely suited here. Frameworks using MPS + MF for Q1D spin [35,36] and bosonic systems [37] have been successfully employed, e.g., in experiments on spin-ladder materials. They compare well to QMC algorithms, despite the MF approximation in the weak-coupling directions, at greatly increased efficiency.

Applying the MPS + MF approach to fermions is more demanding than for spins or bosons, as the MF amplitudes are more numerous than for those systems, which typically have one such amplitude. Moreover, these amplitudes range over multiple sites, raising the bond dimension of the matrix product operator representing the total Hamiltonian. When the 1D subunits have internal structure, as the two-leg Hubbard ladder does, even higher performance is required. Modern MPS implementations can treat even such complex models with many long-range coupling terms, despite the potentially large bipartite entanglement, which sets computational complexity in MPS methods.

Work on DMRG for ground states of 2D Hubbard models demonstrates this fact [9–13,38]. A recent DMRG implementation for distributed-memory architectures, parallel DMRG (pDMRG), can treat very large clusters by MPS standards, of, e.g., the 2D U-V Hubbard models of the Bechgaard and Fabre salts [14]. Yet, calculations for correlated fermions in Q1D systems cannot be handled in this way; the bipartite entanglement in 3D would be far too large. Auxiliary-field QMC (AFQMC) methods [39–42] are applied in this work for the cases with attractive interactions, but they are typically computationally intensive, and in general, the fermionic sign problem prevents exact solutions.

The MF approximation within the MPS + MF scheme for fermions thus allows the present work to study the ground state and thermal properties of much larger correlated Q1D systems, including those with repulsive interactions, than either brute-force MPS methods or AFQMC. Being primarily MPS based, the framework can also be extended to nonequilibrium real-time problems, such as the study of dynamically induced superconductivity in a Q1D system [43].

The present work is structured as follows: Sec. II describes a basic Q1D model of superconductivity, an array of negative-U Hubbard chains, and how to obtain a 1D problem with self-consistent MF amplitudes from it. Section III defines the MPS + MF algorithm used to solve this effective 1D model and motivates its various optimizations. The MF order treated here is a superconducting one, but we briefly discuss how the framework can be extended to address multiple competing orders simultaneously. Then, Sec. IV features an analytical treatment of the same model. In Sec. V, results of the MPS + MF framework are shown. These are compared to analytical methods, and we show how these can be used to obtain T_c from ground-state calculations. Furthermore, we compare our results for a 2D version of our basic Q1D model against AFQMC. Separately, Sec. VI features all the developed tools being used to solve an array of weakly coupled, doped, repulsive-U Hubbard ladders in 3D, whose low-energy properties are analogous to the array of negative-U Hubbard chains, and the T_c for USC is obtained. In Sec. VII, examples of the required resources for running the different presented MPS + MF use cases are presented. Finally, in Sec. VIII the results are discussed and an outlook is given on future work.

II. MODEL

The two related models that are studied in this paper are illustrated in Fig. 1. Both are Q1D arrays in 2D and 3D, comprised of many identical 1D subunits in parallel (e.g., chains and ladders). They are described by a Hamiltonian H_0, and connected by a perturbing Hamiltonian $H_\perp$ with the general form

$$H = H_0 + t_\perp H_\perp. \tag{1}$$

The first model we consider is shown in Fig. 1(a) and permits extensive testing and validation and is treated in Secs. II–V. It features a 3D Hamiltonian with anisotropic tunneling and interactions where H_0 and $H_\perp$ take the following forms:

$$
\begin{aligned}
H_0 &= \sum_{\{\mathbf{R}_i\}} H_0(\mathbf{R}_i) \\
&= -t \sum_{n}^{L-1} \sum_{\{\mathbf{R}_i\},\sigma} (c^\dagger_{n+1,\mathbf{R}_i,\sigma} c_{n,\mathbf{R}_i,\sigma} + \text{H.c.}) \\
&\quad - \mu \sum_{n}^{L} \sum_{\{\mathbf{R}_i\},\sigma} c^\dagger_{n,\mathbf{R}_i,\sigma} c_{n,\mathbf{R}_i,\sigma} + U \sum_{n}^{L} \sum_{\{\mathbf{R}_i\}} n_{n,\mathbf{R}_i,\uparrow} n_{n,\mathbf{R}_i,\downarrow}
\end{aligned}
\tag{2}
$$

and

$$
H_\perp = -\sum_{n}^{L} \sum_{\{\mathbf{R}_i\}} \sum_{\hat{\mathbf{a}}\in\{\hat{\mathbf{y}},\hat{\mathbf{z}}\}} (c^\dagger_{n,\mathbf{R}_i+\hat{\mathbf{a}},\sigma} c_{n,\mathbf{R}_i,\sigma} + \text{H.c.}). \tag{3}
$$

Here, $\{\mathbf{R}_i\}$ indicates a 2D subspace spanned by $\hat{\mathbf{y}}, \hat{\mathbf{z}}$. The operator of $c^\dagger_{n,\mathbf{R}_i,\sigma}$ creates a fermion on site n in a chain at $\mathbf{R}_i$ with spin σ. The parameters t, μ, and U denote hopping, chemical potential, and on-site interaction, respectively. The only higher-dimensional effect in this model is given by $H_\perp$.

The second model we consider is a generalization of the first. It is made up of weakly coupled doped-Hubbard-ladder systems with repulsive interactions shown in Fig. 1(b). The definition of H_0 and $H_\perp$ differ somewhat in appearance from the first and is specified further in Sec. VI and Appendix E. The methods developed to treat the first model in Secs. II–V will be used to treat this latter, more complicated case in Sec. VI.

For both models, there are two fundamental energy scales: the spin gap and the pairing energy. The former measures the cost of energy to flip a spin in a single 1D system at any position $\mathbf{R}_i$. It is defined by

$$
\Delta E_s = E(N, S = 1) - E(N, S = 0), \tag{4}
$$

where $E(N, S)$ is the ground-state energy of $H_0(\mathbf{R}_i)$ (i.e., a single 1D subunit) at charge and spin quantum numbers N and S, respectively. Conversely, the pairing energy is the cost to move one spin from an $S = 0$ chain to a neighboring 1D subunit, also at $S = 0$, creating two chains at $S = 1/2$,

$$
\Delta E_p = 2E\left(N + 1, \frac{1}{2}\right) - E(N, 0) - E(N + 2, 0). \tag{5}
$$

As we see in the following section, these energy scales and, in particular, ΔE_p, for which generally $\Delta E_s \leq \Delta E_p$ (see,

for instance, Ref. [5]), will govern the strength of higher-dimensional effects.

A. Perturbation theory

The models presented in the previous section are typically a challenge to solve numerically and analytically. In particular, the doped Hubbard ladder with repulsive interactions would be impossible to treat in a 3D array of any meaningful size. However, restricting ourselves to the case of the gaps in Eqs. (4) and (5) being large in comparison to the strength of the perturbing Hamiltonian $H_\perp$, we can construct a perturbation theory in the ratio $t_\perp/\Delta E_p$; that is, in order to solve Hamiltonians of the form Eq. (1) we specialize to the case where $t_\perp \ll 2\Delta E_s, \Delta E_p$.

Specifically, when $U < 0$ and $t_\perp = 0$ this model describes a set of disconnected 1D Hamiltonians $H_0(\mathbf{R}_i)$. Each such Hamiltonian exhibits a spectrum of the form

$$
|E_{i,\alpha} - E_{j,\alpha}| \ll |E_{i,\alpha} - E_{j,\beta}|, \quad \alpha \neq \beta, \tag{6}
$$

where α, β indicate changes to the state that induce a large energy shift and i, j small shifts [4]. The labeling is used to distinguish energy states i, j which lie in the same manifold and α, β which denote what manifold the state is in. In the case of our model, this manifold structure is related to a spin-singlet pair forming by the parameter $U < 0$. The subsequent breakup of such pairs by spin flip costs ΔE_s in the isolated 1D system, giving rise to Eq. (6), which is illustrated in Fig. 2. Conversely, when a pair is broken by a process like Eq. (3), two well-separated and unpaired spins are left, which changes this cost to ΔE_p.

When $t_\perp$ is much smaller than the pairing energy, it is possible to produce an effective Hamiltonian with perturbation theory acting in manifold α with matrix elements [44]
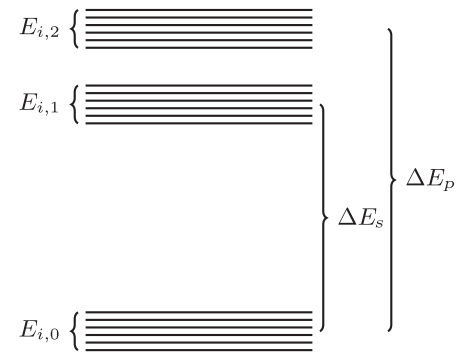

FIG. 2. Schematic representation of the spectrum for Hamiltonians of form Eq. (1) which are considered. The gaps highlighted are the spin gap ΔE_s and pairing energy ΔE_p. Notably, the spin gap and pairing energy are approximated as independent of small variations in energy.

$$\langle i|H_{\text{eff}}^{\alpha}|j\rangle = E_{i,\alpha}\delta_{i,j} + \langle i,\alpha|t_{\perp}H_{\perp}|j,\alpha\rangle + \frac{1}{2}\langle i,\alpha|t_{\perp}H_{\perp}\left(\frac{1}{E_{i,\alpha}-H_0} + \frac{1}{E_{j,\alpha}-H_0}\right)t_{\perp}H_{\perp}|j,\alpha\rangle + \mathcal{O}(t_{\perp}^3). \quad (7)$$

The action of $H_{\perp}$ on $|j,\alpha\rangle$ changes the manifold of the state. We assume that the energy differences between states inside manifolds are much smaller than that of states in different manifolds:

$$E_{i,0} - E_{j,2} \approx -\Delta E_p, \quad (8)$$

where we let $\alpha = 0$ indicate the lowest manifold and $\alpha = 2$ the one reached by $H_{\perp}$. In other words, we approximate the energy difference between states of different manifolds to be independent of the exact state in that manifold. This yields the effective Hamiltonian

$$H_{\text{eff}}^0 = H_0 P_0 + t_{\perp}P_0 H_{\perp}P_0 - \frac{t_{\perp}^2}{\Delta E_p}P_0 H_{\perp}^2 P_0, \quad (9)$$

where $P_{\alpha} = \sum_i |i,\alpha\rangle\langle i,\alpha|$ is a projector onto manifold α. By design, $H_{\perp}$ puts a state in manifold 0 into manifold 2. This means that

$$\langle i,0|t_{\perp}P_0 H_{\perp}P_0|j,\beta\rangle = \langle i,0|t_{\perp}P_0|k,2\rangle = 0. \quad (10)$$

Thus, the first-order and odd-order contribution of the effective Hamiltonian disappears, and we are left with

$$H_{\text{eff}}^0 = H_0 P_0 - \frac{t_{\perp}^2}{\Delta E_p}P_0 H_{\perp}^2 P_0 + \mathcal{O}(t_{\perp}^4). \quad (11)$$

In order to understand how $H_{\perp}^2$ acts on a state, we expand

$$H_{\perp}^2 = \sum_{n,m}^{L} \sum_{\{\mathbf{R}_i,\mathbf{R}_j\}} \sum_{\hat{\mathbf{a}},\hat{\mathbf{b}}\in\{\hat{\mathbf{y}},\hat{\mathbf{z}}\}} \sum_{\sigma,\sigma'} (c_{n,\mathbf{R}_i+\hat{\mathbf{a}},\sigma}^{\dagger} c_{n,\mathbf{R}_i,\sigma} c_{m,\mathbf{R}_j+\hat{\mathbf{b}},\sigma'}^{\dagger} c_{m,\mathbf{R}_j,\sigma'} + c_{n,\mathbf{R}_i+\hat{\mathbf{a}},\sigma}^{\dagger} c_{n,\mathbf{R}_i,\sigma} c_{m,\mathbf{R}_j,\sigma'}^{\dagger} c_{m,\mathbf{R}_j+\hat{\mathbf{b}},\sigma'}$$
$$+ c_{n,\mathbf{R}_i,\sigma}^{\dagger} c_{n,\mathbf{R}_i+\hat{\mathbf{a}},\sigma} c_{m,\mathbf{R}_j+\hat{\mathbf{b}},\sigma'}^{\dagger} c_{m,\mathbf{R}_j,\sigma'} + c_{n,\mathbf{R}_i,\sigma}^{\dagger} c_{n,\mathbf{R}_i+\hat{\mathbf{a}},\sigma} c_{m,\mathbf{R}_j,\sigma'}^{\dagger} c_{m,\mathbf{R}_j+\hat{\mathbf{b}},\sigma'}), \quad (12)$$

obtaining a Hamiltonian describing two-particle tunneling events. What characterizes the $\alpha = 0$ manifold is pair formation of opposite spins due to attractive interaction. Some terms within $H_{\perp}^2$ will put the state in a manifold $\beta > \alpha$ and will subsequently be projected out. Most importantly, any terms flipping spins in two chains simultaneously, such as $c_{n,\mathbf{R}_i,\uparrow}^{\dagger} c_{n,\mathbf{R}_i+\hat{\mathbf{y}},\uparrow} c_{n,\mathbf{R}_i+\hat{\mathbf{y}},\downarrow}^{\dagger} c_{n,\mathbf{R}_i,\downarrow}$, which would move two chains initially in their $S = 0$ manifolds into their $S = \pm 1$ manifolds, will be projected out due to describing a state with at least energy $2\Delta E_s$ above the lowest-energy manifold. In this manner, it is clear that each chain in our model has to conserve spin and in particular pair all spins such that total spin $S = 0$.

The parts of $H_{\perp}^2$ which remain after projecting to $\alpha = 0$ must either move particles as pairs (simultaneous tunneling of an up-spin and down-spin particle) or exchange them between chains (an up- or down-spin particle is moved out of the chain and another of the same spin is moved in). Any of these processes involve at most two chains in order to conserve spin. While $H_{\perp}^2$ allows for processes involving chains at arbitrary distance, these would concern four separate chains, with a final state at least $2\Delta E_p$ above the low-energy manifold, and thus removed by projection.

With these restrictions, $H_{\perp}^2$ becomes heavily reduced:

$$H_{\perp}^2 = \sum_{n,m}^{L} \sum_{\{\mathbf{R}_i\}} \sum_{\hat{\mathbf{a}}\in\{\hat{\mathbf{y}},\hat{\mathbf{z}}\}} \sum_{\sigma} (c_{n,\mathbf{R}_i+\hat{\mathbf{a}},\sigma}^{\dagger} c_{n,\mathbf{R}_i,\sigma} c_{m,\mathbf{R}_i+\hat{\mathbf{a}},-\sigma}^{\dagger} c_{m,\mathbf{R}_i,-\sigma} + c_{n,\mathbf{R}_i,\sigma}^{\dagger} c_{n,\mathbf{R}_i+\hat{\mathbf{a}},\sigma} c_{m,\mathbf{R}_i,-\sigma}^{\dagger} c_{m,\mathbf{R}_i+\hat{\mathbf{a}},-\sigma})$$

$$+ \sum_{n,m}^{L} \sum_{\{\mathbf{R}_i\}} \sum_{\hat{\mathbf{a}}\in\{\hat{\mathbf{y}},\hat{\mathbf{z}}\}} \sum_{\sigma} (c_{n,\mathbf{R}_i+\hat{\mathbf{a}},\sigma}^{\dagger} c_{n,\mathbf{R}_i,\sigma} c_{m,\mathbf{R}_i,\sigma}^{\dagger} c_{m,\mathbf{R}_i+\hat{\mathbf{a}},\sigma} + c_{n,\mathbf{R}_i,\sigma}^{\dagger} c_{n,\mathbf{R}_i+\hat{\mathbf{a}},\sigma} c_{m,\mathbf{R}_i+\hat{\mathbf{a}},\sigma}^{\dagger} c_{m,\mathbf{R}_i,\sigma})$$

$$= H_{\text{pair}} + H_{\text{exc}}. \quad (13)$$

The first set of operators H_{pair} corresponds to pairs of fermions jumping from one chain to another. This conserves spin but not the number of particles within a chain. The second set of operators H_{exc} corresponds to fermions of like spin switching chains (not necessarily at the same site within a chain).

Within this Hamiltonian, there is still the degree of freedom to pick how large $|n - m|$ we include. This is something that cannot be restricted by symmetry arguments or the smallness of $t_\perp/\Delta E_p$.

B. Mean-field theory

Notably, the perturbation theory has produced an effective quartic interaction from the single-particle tunneling Hamiltonian. This can be further simplified by casting Eq. (13) in a form where there is no explicit mention of other chains. This allows us to solve an effective 1D model instead of the full 3D system. We use an ansatz of quasifree states:

$$\langle c_i^\dagger c_j^\dagger c_k c_l \rangle = \langle c_i^\dagger c_j^\dagger \rangle \langle c_k c_l \rangle + \langle c_i^\dagger c_l \rangle \langle c_j^\dagger c_k \rangle - \langle c_i^\dagger c_k \rangle \langle c_j^\dagger c_l \rangle, \tag{14}$$

which produces a mean-field Hamiltonian from the quartic operators in Eq. (13). We further approximate the expectation value of any operator creating or annihilating particles on two different chains to zero; i.e., pair constituents cannot live on different chains. This is motivated by choosing small enough $t_\perp/\Delta E_p$, amounting to the standard mean-field approximation.

1. Pairing terms

For each chain $\mathbf{R}_i$ of the pair-hopping Hamiltonian H_{pair}, we obtain

$$
\begin{aligned}
H_{\text{pair,MF}} = &-\sum_{n,m}^{L} \sum_{\hat{\mathbf{a}} \in \{\hat{\mathbf{y}},\hat{\mathbf{z}}\}} \sum_\sigma (\langle c_{n,\mathbf{R}_i+\hat{\mathbf{a}},\sigma}^\dagger c_{m,\mathbf{R}_i+\hat{\mathbf{a}},-\sigma}^\dagger \rangle c_{n,\mathbf{R}_i,\sigma} c_{m,\mathbf{R}_i,-\sigma} + c_{n,\mathbf{R}_i,\sigma}^\dagger c_{m,\mathbf{R}_i,-\sigma}^\dagger \langle c_{n,\mathbf{R}_i+\hat{\mathbf{a}},\sigma} c_{m,\mathbf{R}_i+\hat{\mathbf{a}},-\sigma} \rangle \\
&+ \langle c_{n,\mathbf{R}_i-\hat{\mathbf{a}},\sigma}^\dagger c_{m,\mathbf{R}_i-\hat{\mathbf{a}},-\sigma}^\dagger \rangle c_{n,\mathbf{R}_i,\sigma} c_{m,\mathbf{R}_i,-\sigma} + c_{n,\mathbf{R}_i,\sigma}^\dagger c_{m,\mathbf{R}_i,-\sigma}^\dagger \langle c_{n,\mathbf{R}_i-\hat{\mathbf{a}},\sigma} c_{m,\mathbf{R}_i-\hat{\mathbf{a}},-\sigma} \rangle) \\
= &\, 2z_c \sum_{n,m}^{L} (\langle c_{n,\uparrow} c_{m,\downarrow} \rangle c_{n,\uparrow} c_{m,\downarrow} + \langle c_{n,\uparrow} c_{m,\downarrow} \rangle c_{m,\downarrow}^\dagger c_{n,\uparrow}^\dagger),
\end{aligned}
\tag{15}
$$

where $z_c = 4$ is the coordination number for three dimensions. Notably, the mean field is performed on two dimensions instead of the full three. We assume that

$$
\begin{aligned}
\langle c_{n,\uparrow} c_{m,\downarrow} \rangle = \langle c_{m,\downarrow}^\dagger c_{n,\uparrow}^\dagger \rangle &= \langle c_{n,\mathbf{R}_i,\uparrow} c_{m,\mathbf{R}_i,\downarrow} \rangle \\
&= \langle c_{n,\mathbf{R}_i+p\hat{\mathbf{a}},\uparrow} c_{m,\mathbf{R}_i+p\hat{\mathbf{a}},\downarrow} \rangle, \quad \forall \ p \in \mathbb{N}, \quad \hat{\mathbf{a}} \in \{\hat{\mathbf{y}}, \hat{\mathbf{z}}\},
\end{aligned}
\tag{16}
$$

i.e., that all chains are identical and the mean field is real valued.

2. Exchange terms

For each chain $\mathbf{R}_i$ of the exchange Hamiltonian H_{exc}, we obtain

$$
\begin{aligned}
H_{\text{exc,MF}} = &-\sum_{n,m}^{L} \sum_{\hat{\mathbf{a}} \in \{\hat{\mathbf{y}},\hat{\mathbf{z}}\}} \sum_\sigma (\langle c_{n,\mathbf{R}_i+\hat{\mathbf{a}},\sigma}^\dagger c_{m,\mathbf{R}_i+\hat{\mathbf{a}},\sigma} \rangle c_{m,\mathbf{R}_i,\sigma}^\dagger c_{n,\mathbf{R}_i,\sigma} + \langle c_{n,\mathbf{R}_i-\hat{\mathbf{a}},\sigma}^\dagger c_{m,\mathbf{R}_i-\hat{\mathbf{a}},\sigma} \rangle c_{m,\mathbf{R}_i,\sigma}^\dagger c_{n,\mathbf{R}_i,\sigma} \\
&+ \langle c_{m,\mathbf{R}_i+\hat{\mathbf{a}},\sigma}^\dagger c_{n,\mathbf{R}_i+\hat{\mathbf{a}},\sigma} \rangle c_{n,\mathbf{R}_i,\sigma}^\dagger c_{m,\mathbf{R}_i,\sigma} + \langle c_{m,\mathbf{R}_i-\hat{\mathbf{a}},\sigma}^\dagger c_{n,\mathbf{R}_i-\hat{\mathbf{a}},\sigma} \rangle c_{n,\mathbf{R}_i,\sigma}^\dagger c_{m,\mathbf{R}_i,\sigma}) \\
= &-z_c \sum_{n,m}^{L} \sum_\sigma (\langle c_{n,\sigma}^\dagger c_{m,\sigma} \rangle c_{m,\sigma}^\dagger c_{n,\sigma} + \langle c_{m,\sigma}^\dagger c_{n,\sigma} \rangle c_{n,\sigma}^\dagger c_{m,\sigma}) \\
= &-2z_c \sum_n^{L} \sum_{r=1}^{L-n} \sum_\sigma (\langle c_{n,\sigma}^\dagger c_{n+r,\sigma} \rangle c_{n+r,\sigma}^\dagger c_{n,\sigma} + \langle c_{n+r,\sigma}^\dagger c_{n,\sigma} \rangle c_{n,\sigma}^\dagger c_{n+r,\sigma}),
\end{aligned}
\tag{17}
$$

which is similar to what we do in Eq. (16).

C. Effective 1D Hamiltonian

To summarize: Within the MPS + MF approach, the total Hamiltonian is described by its one-dimensional subsets in a mean-field sense. It is sufficient to consider the effectively 1D Hamiltonian

$$H_{\mathrm{MF}} = H_0(\mathbf{R}_i) - \sum_{i,k} \alpha_{i,k}(c_{i,\uparrow} c_{k,\downarrow} + c_{k,\downarrow}^\dagger c_{i,\uparrow}^\dagger)$$
$$+ \sum_{i,\sigma} \sum_{r=1}^{L-i} \beta_{i,r,\sigma}(c_{i+r,\sigma}^\dagger c_{i,\sigma} + c_{i,\sigma}^\dagger c_{i+r,\sigma}), \quad (18)$$

where

$$\alpha_{i,k} = \frac{2z_c t_\perp^2}{\Delta E_p} \langle c_{i,\uparrow} c_{k,\downarrow} \rangle \quad (19)$$

are the pair-MF parameters describing pair tunneling into or out of the 1D system mediated by H_{pair}, and

$$\beta_{i,r,\sigma} = \frac{2z_c t_\perp^2}{\Delta E_p} \langle c_{i+r,\sigma}^\dagger c_{i,\sigma} \rangle \quad (20)$$

are the exchange processes mediated by H_{exc} [cf. Eq. (13)]. Notably, $\alpha_{i,k}$ is proportional to the bound-state-pair wave function. In practice, keeping all ranges will make the problem intractable and limits must be introduced. Fortunately, the existence of a spin gap causes α and β to decay exponentially with distance controlled by the spin correlation length [4]. This allows us to include a cutoff for which amplitudes to keep. The choice of this value ultimately depends on microscopic parameters (in particular, interaction strength) and is exemplified in Sec. V.

In addition, it is important to note that the zero-range terms $\beta_{i,0,\sigma} \propto \langle n_{i,\sigma} \rangle$ are absent in H_{MF} as we assume constant density in the superconducting order and exclude potential insulating orders. We have already extended the MPS + MF framework to study the competition of insulating charge orders with superconducting ones, based on adding $\beta_{i,0,\sigma}$ parameters, and are applying this to the Hubbard-ladder arrays in forthcoming work.

Finally, as we discuss in Sec. II A, MF terms such as $\langle S_i^+ \rangle S_i^-$ cannot occur in H_{MF} by construction, as such magnetic exchange terms are suppressed through the condition that $k_B T \ll \Delta E_s$ for thermal fluctuations and $t_\perp \ll 2\Delta E_s$ at zero temperature.

III. MPS + MF: NUMERICAL SOLUTIONS TO Q1D SYSTEMS USING MEAN-FIELD THEORY

MPS + MF is developed to solve Q1D models by relying on mean-field approximations of the full Hamiltonian which converts it to an effectively 1D system. The produced Hamiltonian in Eq. (18) may be solved iteratively until self-consistency is reached for the mean-field amplitudes as shown schematically in Fig. 3.

This framework is developed as an approach to anisotropic systems in two or more dimensions for which the 1D correlations are most important and where single-particle tunneling and spin-flipping processes between chains can be neglected on account of $t_\perp \ll \Delta E_p$. The primary cost of the routine comes from the repeated solutions of effective 1D mean-field Hamiltonian such as Eq. (18) using MPS-based methods. Notably, any MPS method may be used to iterate mean-field amplitudes, for example, original DMRG, MPS-based DMRG, or imaginary-time evolution on purified states to obtain thermal states. In practice, the only requirement is that the mean-field amplitudes converge. Thus, the framework scales as the utilized DMRG method does with bond dimension and system size [32]. The actual run-time can be shortened by exploiting
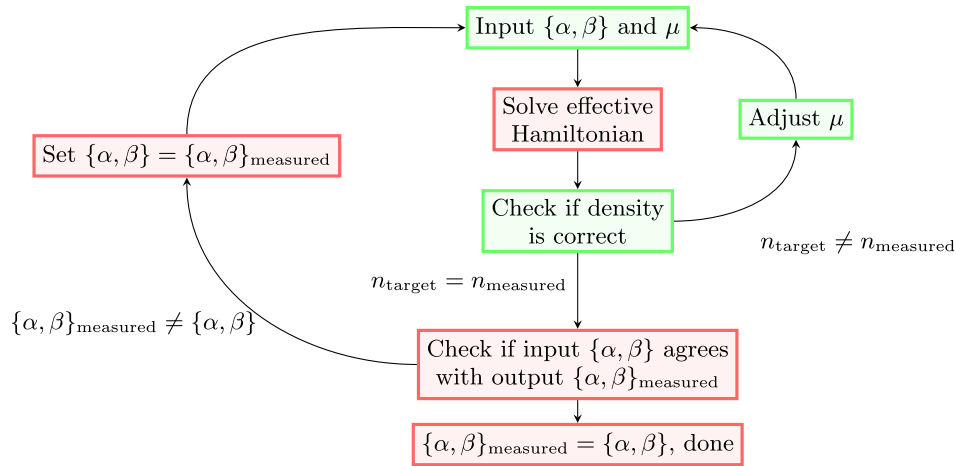

FIG. 3. Schematic representation of the MPS + MF framework. Green boxes highlight the density-fixation part of the routine. Red boxes denote the mean-field amplitude fixation part. The mean-field amplitude set is denoted by $\{\alpha, \beta\}$ where $\{\alpha\}$ represent pairing amplitudes and $\{\beta\}$ the exchange amplitudes.
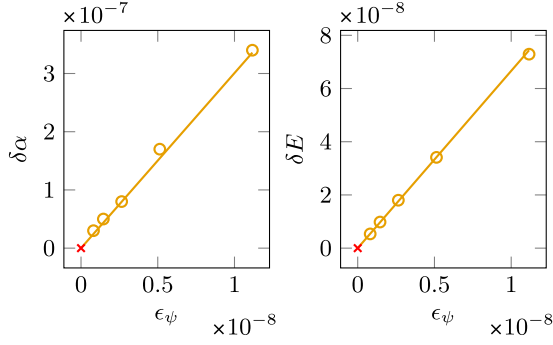
FIG. 4. Example of truncation error extrapolation of order parameter and ground-state energy for a chain of length $L = 100$ at attractive interaction $U = -4t$ and density $n = 0.5$ and $t_\perp = 0.05t$. The y axes represent difference of order parameter $\delta\alpha = \alpha(\epsilon_\psi) - \alpha(0)$ and similarly for energy. The range of MF terms taken into account is $r = 4$.

conserved quantities; for our calculations, we exploit the spin quantum number S as a U(1) symmetry. In this paper, we utilize MPS-based DMRG to solve for ground states [32]. For thermal states, we utilize both Trotterized imaginary-time evolution and the time-dependent variational principle (TDVP) [45].

One common feature of states obtained with DMRG ground-state algorithms is that the error of local quantities scales linearly with the discarded weight [46]. Given that the system under study is 1D, albeit representing a 3D system, we might expect that such a linear scaling holds for MPS + MF as well. In Fig. 4, we show an example of our general finding that this holds true for quantities such as energy and order parameter.

A. Achieving self-consistent convergence

When iterating a MF theory to self-consistency, the required number of iterations becomes crucial as each one may have significant cost. We consider a state converged when the previous iteration's self-consistent values agree with the current iteration within the desired tolerance. For this paper, the relative tolerance required for a converged state is chosen as

$$\frac{|\alpha_n - \alpha_{n-1}|}{|\alpha_{n-1}|} < 10^{-4}, \tag{21}$$

where α_n indicates any self-consistent value at iteration n. The number of solutions required to achieve a self-consistent state is not constant over parameter space as shown in Fig. 5(a). However, it varies only modestly with Hamiltonian parameters, such as $t_\perp$. The notable increase in loop number with larger $t_\perp$ is primarily due to increased difficulty fixing the density (see Sec. III D). Furthermore, we find that the number of required iterations peaks strongly around the phase transition from the superconducting to normal phase as shown in Fig. 5(b) where the
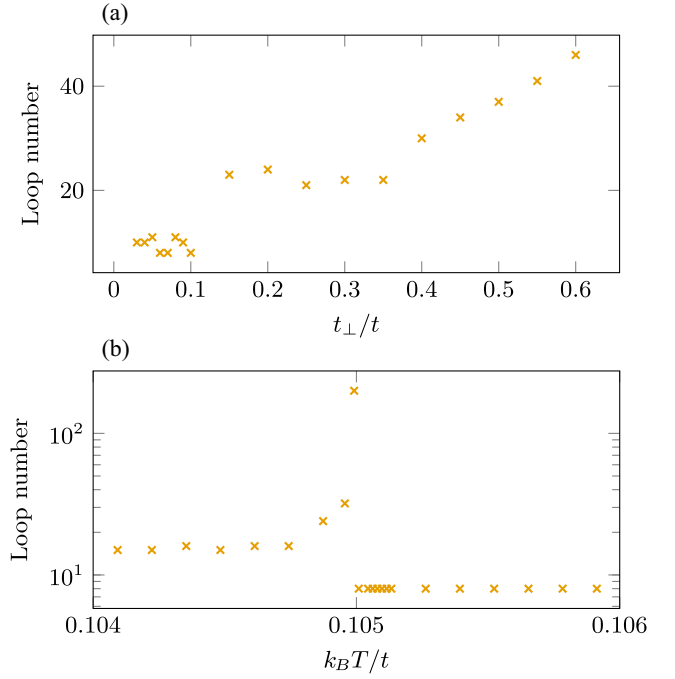

FIG. 5. Number of self-consistent loops required for convergence for (a) a ground-state calculation for different values $t_\perp$ at $L = 100$, $n = 0.5$, $U = -4t$, $\chi = 300$, and MF term range $r = 4$, and (b) a finite-temperature calculation for different temperatures at $L = 60$, $n = 0.5$, $U = -10t$, $t_\perp = 0.3t$, $\chi = 200$, and MF terms with range $r = 1$.

transition occurs around $T = 0.105$ [37,47,48]. When the superconductor is close to its transition to a metal, the MF coupling between chains is weak but nonzero. We find this slows down the convergence rate, explaining the increase in the number of required loops for convergence.

In both this work and the primary uses to which the MPS + MF framework would be applied, the interest in phase transitions is central, and we have to resolve the points which are difficult to obtain. This prompts the development of several heuristics in this method to produce a faster convergence.

B. Extrapolation

Convergence implies that the mean-field amplitudes approach a set which no longer changes with further iteration; i.e., the change of these amplitudes with each iteration decreases. As can be seen from Fig. 6, we find such an exponential behavior after an initial fluctuation (related to the initial guess). Given the clear trend, an extrapolation can be performed to attempt a prediction of the converged amplitudes.

In practice, such fits seldom give precise results but typically lead to a more converged amplitude compared to simply iterating one more loop. As such, we employ a strategy of repeated extrapolation in an attempt to speed up the self-consistent iteration as shown in Fig. 6. The result of
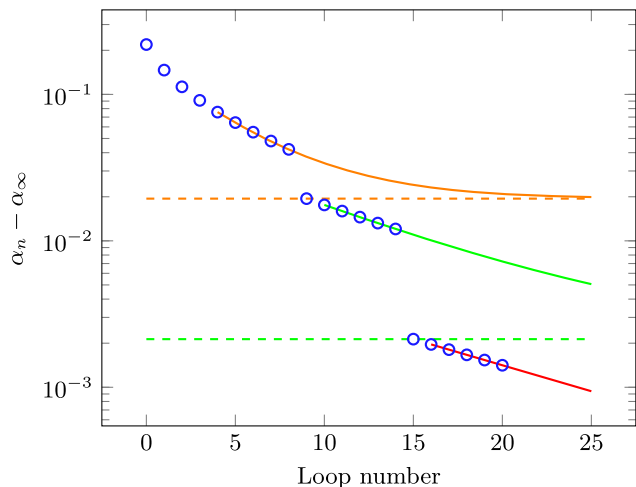
FIG. 6. Example of the exponential trend when iterating to self-consistency. The mean-field amplitude over loop number n is denoted by α_n and converged amplitude [as defined by Eq. (21)] by α_∞. The system parameters are $L = 60$, $U = -10t$, $t_\perp = 0.4t$, $\beta t = 6.4286$, $\chi = 200$, and MF terms with range $r = 1$.

five consecutive iterations is checked for sufficient exponential behavior and is fitted to an exponential function

$$f(x) = Ae^{-|B|x} + C, \qquad (22)$$

where the fitting parameters A, B, C are determined by a least-squares fit. In this manner, C is the fitted result when approaching infinite iterations and is chosen as the amplitude to use for the next iteration.

Typically, we find that this scheme reduces the number of necessary iterations to a varying degree. In particular, close to transitions, the slow convergence can be greatly aided by skipping ahead using extrapolations. In effect, the scheme is a method of breaking off the iterative procedure in order to generate an improved initial guess using exponential extrapolation. The amount of speedup depends on how evenly and slowly the mean-field amplitudes converge. If the convergence is quick, fitting to an exponential form is less faithful. Conversely, if convergence is too slow the extrapolated result makes predictions far outside any region of reliability (e.g., using ten iterations to predict what would happen after 1000 iterations). In the best-case scenarios, we find the number of iterations reduced by up to a factor of 5, and in the worst case, it executes only once or not at all leading to small or no speedup.

C. Initial guesses

As shown in Fig. 3, the routine has to be started with some input mean-field amplitudes and chemical potential. This indicates that the number of DMRG solutions is dependent on the quality of the initial guess. In certain cases, bosonization can be used to make estimations of

what the converged amplitudes would be, in particular, where analytical control is good. However, in general, such estimations will differ from the DMRG result and are often harder to obtain than simple heuristic guesses.

What is always available for initial values is that of previous solutions using the framework. Indeed, the best guess is the set of converged amplitudes leading to an immediate solution. This becomes useful when considering that mean-field amplitudes should often change only marginally when subject to a marginal shift in parameter space (a notable exception is that of first-order transitions). Hence, if we seek a point in parameter space that is close to one which is already computed, the converged amplitudes of the computed point serve as a guess which should be close to the converged result.

This observation is of particular use when considering the bond dimension. DMRG scales cubically in this quantity [32]. It is imperative to keep this parameter large enough in order for the obtained state to reasonably approximate the targeted state. With the MPS + MF framework it is possible to compute the self-consistent amplitudes at a lower bond dimension starting with unguided guesses at low cost. When high precision is desired, we use the cheap results to compute amplitudes at higher bond dimension. We find that the number of required iterations performed at higher bond dimension drops significantly with this strategy, as exemplified in Fig. 7. Thus, we start by converging the lowest bond dimension considered. Subsequently, the higher bond dimensions are launched with the converged values of the lowest bond dimension.

Furthermore, this strategy may be applied to the issue of phase transitions. For such cases, a dense grid of data is
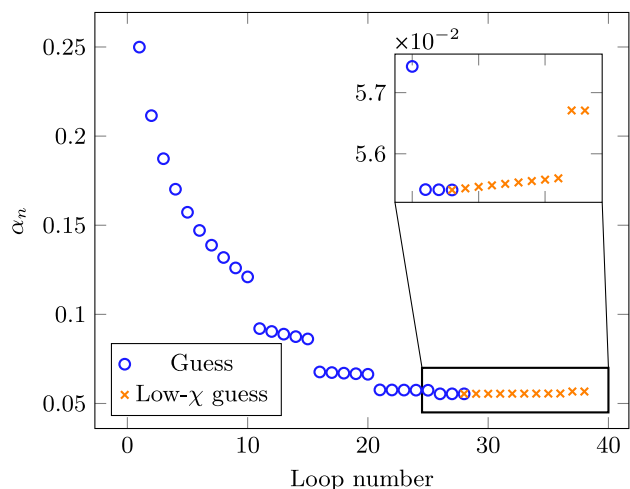

FIG. 7. Comparison of loop count n and mean-field amplitude α_n when using a simple, unguided guess at bond dimension $\chi = 100$ and when using the $\chi = 100$ converged amplitudes as a guess for $\chi = 200$. The system parameters are $L = 60$, $U = -10t$, $t_\perp = 0.3t$, $\beta t = 9.5948$, and $\chi = 100$ (blue circles) and $\chi = 200$ (orange crosses). The MF terms in both cases have range $r = 1$.

often necessary with amplitudes varying only modestly between points. Once a grid of some sparsity has been generated, a tighter one is cheaper due to the possibility of interpolating between existing points, providing good initial guesses.

D. Density fixing

While the original Hamiltonian Eq. (1) is explicitly particle number conserving, the derived effective 1D Hamiltonian Eq. (18) loses this property. Since carrier density has been shown to affect superconductivity, it is important to consider what density the converged solution obtains. In practice, being able to fix the density is important, since there is no guarantee that converged solutions at different parameters have the same density thereby making comparison difficult.

In Fig. 3, two classes of amplitudes are considered: $\{\alpha, \beta\}$, which represent the set of mean-field amplitudes, and μ, the chemical potential, which may be used to control the density of the system. However, there is no way to determine which chemical potential to use for a given density. In previous applications, this issue was resolved by sampling a grid of exact data from exact diagonalization on small systems in order to obtain a range of μ in which interpolation to high precision was possible [37].

For models considered in this work, the number of mean-field amplitudes is too great to attempt such a solution. Instead, a heuristic algorithm is designed to obtain the appropriate density as shown in Fig. 8. In essence, the algorithm attempts to find a chemical potential μ_{target} such that

$$n(\mu_{\text{target}}) = n_{\text{target}}, \tag{23}$$

where computing the density $n(\mu)$ for different μ necessitates a full DMRG solution leading to a significant time

cost. To alleviate this issue, we assume that $n(\mu)$ is a monotonic function of μ and look for a range in which $n(\mu) = n_{\text{target}}$. Once obtained, we use the secant method to narrow the range until the desired tolerance is achieved. In this paper, we require a relative tolerance of

$$\frac{|n_{\text{target}} - n(\mu)|}{n_{\text{target}}} < 10^{-5}. \tag{24}$$

It is notable that the density-fixing routine is most important when the mean-field amplitudes are strongly varying with each iteration. When approaching the self-consistently converged solution, the density typically changes modestly, allowing for loops without running the density-fixing subroutine.

E. Self-consistent excited states

In a superconducting system, much information can be obtained from the energy gap between the ground and the first excited state. This is especially true in Q1D systems, as shown in Sec. IV analytically and confirmed numerically in Sec. V C. Strikingly, finite-temperature properties such as superconducting T_c can be obtained from this gap with minimal computational effort, which is readily exploited in Sec. VI. Thus, we employ the ability of DMRG to compute the lowest-lying eigenstates orthogonal to the ground state. This allows the computation of the first excited-state energy

$$E_{\text{exc}} = \langle \psi_1 | H | \psi_1 \rangle, \qquad \langle \psi_0 | \psi_1 \rangle = 0, \tag{25}$$

where $|\psi_1\rangle$ is the first excited state which minimizes the energy E_{exc} with the constraint that it is orthogonal to $|\psi_0\rangle$, the ground state. The excitation gap may then be defined as

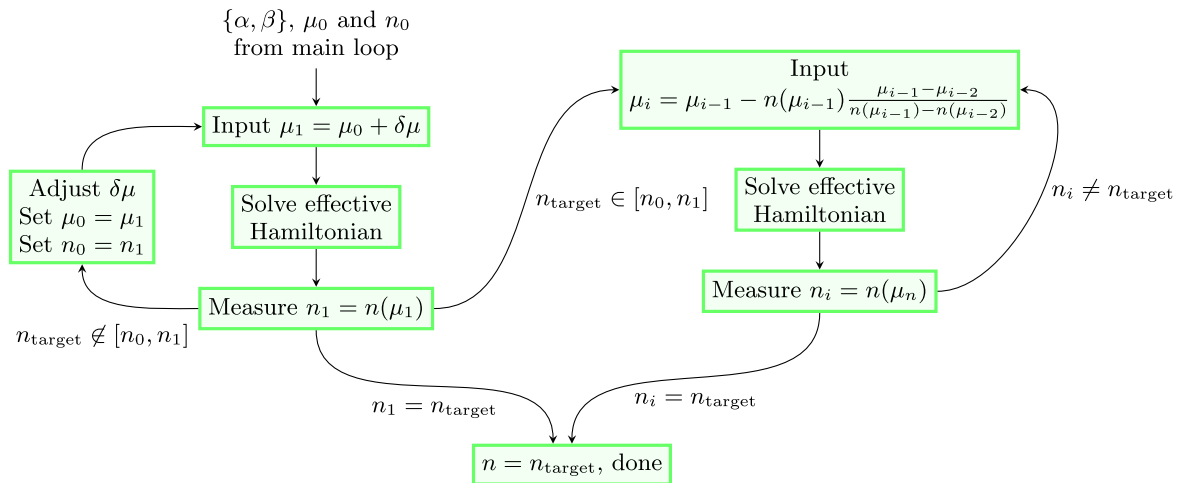$$\Delta = E_{\text{exc}} - \langle \psi_0 | H | \psi_0 \rangle. \tag{26}$$

FIG. 8. Schematic representation of the density-fixing routine. Chemical potential at different stages of the loop are named μ_i and density n_i.
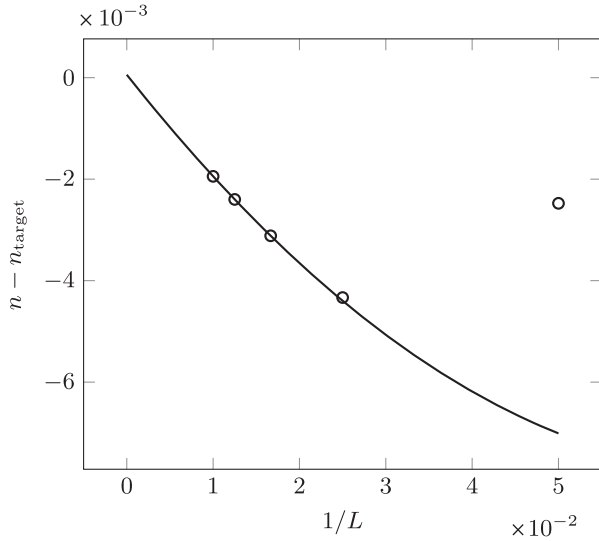
FIG. 9. Example of excited-state density extrapolated to infinite system size for $U = -2t$, $t_\perp = 0.08t$, and density $n_{target} = 0.5$.

The excited state will not generally obey the self-consistency constraint, i.e., mean-field amplitudes measured in the excited state

$$\alpha_{measured} \neq \alpha, \qquad (27)$$

where α is the self-consistent amplitude obtained for the ground state. This means our numerics indicate a depletion of the ground state of condensed pairs, in line with earlier analytical theory [48].

Depletion of pairing can be a concern as the Hamiltonian Eq. (18) does not conserve density. Using the above procedure will yield whatever state of lowest energy that is orthogonal to the ground state and could well be at another density, as is exemplified in Fig. 9.

At the same time, the data also show the deviation decreasing with system size. An extrapolation may thus be performed using a general form of finite-size behavior

$$n(L) = n_\infty + \frac{c_0}{L} + \frac{c_1}{L^2} + \mathcal{O}\left(\frac{1}{L^3}\right). \qquad (28)$$

Thus, we assume that energy gaps extrapolated to infinite-size systems are comparisons of energy at the same density, despite the fact that finite-size-system densities generally differ. This strategy is verified in Sec. V C and Fig. 11, as two methods to obtain superconducting T_c, one purely numeric, the other using Δ, and the field theory of Sec. IV are shown to coincide.

The upshot is that once a self-consistent Hamiltonian has been produced from MPS + MF for ground states, excited states will cost no more than one additional DMRG run, making the computation of Δ relatively cheap.

IV. FIELD THEORY DESCRIPTION

Let us now turn to a field theory analysis of the Hamiltonian Eq. (2). In 1D systems, the effects of inter-actions are dramatically amplified. Additionally, in 1D the quantum and thermal fluctuations prevent the breaking of continuous symmetries [49]. The combination of these effects leads to a unique universality class for interacting 1D quantum systems known as TLLs [50].

The low-energy physics of TLLs can be described in terms of two bosonic fields ϕ and θ related to collective excitations of density and currents. These field are related by the canonical relation

$$[\phi(x), \nabla\theta(x')] = i\pi\delta(x - x'), \qquad (29)$$

which expresses the duality in 1D between density and phase fluctuations. In this bosonized representation, the single-particle fermionic operator of fermions with spin ν reads

$$\psi_\nu(x) = e^{ik_F x}\psi_{R,\nu}(x) + e^{-ik_F x}\psi_{L,\nu}(x), \qquad (30)$$

where $\psi_{R,L,\nu}(x)$ are slowly varying fields describing exci-tations close to the Fermi points $\pm k_F$ (right and left movers), and $\nu = \uparrow, \downarrow$ denotes the spin. These fields are expressed as [4]

$$\psi_{r,\nu}(x) = \frac{U_{r,\nu}}{\sqrt{2\pi\alpha}} e^{-\frac{i}{\sqrt{2}}[r\phi_\rho(x)-\theta_\rho(x)+\nu(r\phi_\sigma(x)-\theta_\sigma(x))]}, \qquad (31)$$

where $U_{r,\nu}$ are Klein factors, $r = R, L$, and α is a cutoff proportional to the lattice spacing, which simulates a finite bandwidth. The fields $\phi_{\rho,\sigma}$ are given by

$$\phi_\rho(x) = \frac{1}{\sqrt{2}}[\phi_\uparrow(x) + \phi_\downarrow(x)],$$

$$\phi_\sigma(x) = \frac{1}{\sqrt{2}}[\phi_\uparrow(x) - \phi_\downarrow(x)], \qquad (32)$$

and similarly for the field θ. In the basis $\{\theta_{\rho,\sigma}, \phi_{\rho,\sigma}\}$, the 1D Hubbard model has the peculiarity of decoupling charge and spin sectors:

$$\mathcal{H} = \mathcal{H}_\rho + \mathcal{H}_\sigma. \qquad (33)$$

Away from half filling (one particle per site) and for negative interactions $U < 0$, the spin sector is gapped while the charge sector is gapless. In the bosonic language, the gapless Hamiltonian is the universal TLL Hamiltonian

$$\mathcal{H}_\rho = \frac{u_\rho}{2\pi} \int dx \left(K_\rho (\nabla\theta_\rho(x))^2 + \frac{1}{K_\rho}(\nabla\phi_\rho(x))^2 \right), \qquad (34)$$

and the spectrum is linear $\omega = u_\rho |k|$. Such a Hamiltonian is fully described by two nonuniversal parameters which

depend on the microscopic model: u_ρ the charge velocity of the collective excitation and K_ρ the Luttinger parameter that controls the algebraic decay of the correlations [4].

On the contrary, the gapped sector is described by a sine-Gordon Hamiltonian which, with respect to Eq. (34), has an additional term proportional to $\cos{(2\sqrt{2}\phi_\sigma)}$ that wants to lock the field ϕ_σ to one of its minima:

$$\mathcal{H}_\sigma = \frac{u_\sigma}{2\pi}\int dx\left(K_\sigma(\nabla\theta_\sigma(x))^2 + \frac{1}{K_\sigma}(\nabla\phi_\sigma(x))^2\right)$$
$$+ \frac{2U}{(2\pi\alpha)^2}\int dx\cos{[2\sqrt{2}\phi_\sigma(x)]}. \tag{35}$$

Physically, it means that the system tends to form Cooper pairs with opposite spins and as a direct consequence suppresses spin excitations. The energy of the bound state is the gap Δ_σ in the spin sector. Notably, Δ_σ is kept distinct in notation from ΔE_s in Eq. (4) as their definitions differ. The field theory spin gap can be computed from the sine-Gordon model by various methods [4] and is exactly known for the microscopic attractive Hubbard model with $U < 0$ by Bethe ansatz [51].

As we describe in the previous sections, we assume here that the spin gap Δ_σ is larger than the interchain coupling $t_\perp$. Our system thus has a low- and high-energy sector. The former relative to hopping in the transverse direction $(t_\perp \ll t)$ and the latter to break the pairs.

Let us first consider the case when $\Delta_\sigma \gg t$ (or $|U| \gg t$). In this case, it is necessary to eliminate the spin sector before bosonizing the Hamiltonian. This can be achieved by a Schrieffer-Wolff transformation [52]. The resulting Hamiltonian is rewritten as

$$\mathcal{H} \sim \mathcal{H}_0 + t_\perp\mathcal{H}_\perp$$
$$= \mathcal{H}_0 - \frac{t_\perp^2}{\Delta_\sigma}\sum_{\langle \mathbf{R},\mathbf{R}'\rangle}\sum_{n,n',s}[c_{n,\mathbf{R}',s}^\dagger c_{n,\mathbf{R},s}c_{n',\mathbf{R}',-s}^\dagger c_{n',\mathbf{R},-s} + \text{H.c.}],$$
$$\tag{36}$$

where $\mathcal{H}_0$ is the 1D quadratic Hamiltonian Eq. (34). The effective coupling is now proportional to the gained energy over the cost of breaking the pair $t_\perp^2/\Delta_\sigma$, and indeed it expresses local pairs hopping in the transverse direction. The spin excitations are exponentially suppressed, while the charge sector is massless. In Eq. (36), we neglect the terms corresponding to the formation of charge-density wave (CDW), because the superconductive correlation (SS) decays slower. Indeed, the corresponding correlations are [4]

$$\langle O_{\text{SS}}^\dagger(r)O_{\text{SS}}(0)\rangle \sim \left(\frac{1}{r}\right)^{\frac{1}{K_\rho}},$$

$$\langle O_{\text{CDW}}^\dagger(r)O_{\text{CDW}}(0)\rangle \sim \left(\frac{1}{r}\right)^{K_\rho}, \tag{37}$$

where the corresponding operators are defined as $O_{\text{CDW}} = \psi_{R,\uparrow}^\dagger\psi_{L,\uparrow} + \psi_{R,\downarrow}^\dagger\psi_{L,\downarrow}$ and $O_{\text{SS}} = \psi_{R,\uparrow}^\dagger\psi_{L,\downarrow}^\dagger + \psi_{L,\uparrow}^\dagger\psi_{R,\downarrow}^\dagger$. For negative U, the TLL charge parameter is larger than 1, $K_\rho > 1$, meaning that CDW formation is a subdominant instability. By using Eq. (36) and considering the leading terms $n = n'$, since the spin gap is larger than the bandwidth (approximation of local pairs), we now use the mean-field approximation whose order parameter reads

$$\langle \psi_{\mathbf{R},\uparrow}^\dagger(x)\psi_{\mathbf{R},\downarrow}^\dagger(x)\rangle = Ce^{-i\sqrt{2}\theta_\rho(x)}, \tag{38}$$

with C a constant that depends on the spin gap Δ_σ but is of order one in this regime (see Appendix G). In this limit, since only the charge sector survives, the problem maps onto a system of hard-core bosons (Cooper pairs) with a transverse hopping described by the field $\sqrt{2}\theta(x)$ instead of $\theta(x)$. Indeed, the physics is similar: The Pauli principle forbids having two pairs in the same site, and two hard-core bosons never occupy the same site.

All chains are now identical, and, in the bosonized version, the 1D effective Hamiltonian reads

$$\mathcal{H} = \mathcal{H}_\rho - \rho_0^2 C^2\frac{t_\perp^2}{\Delta_\sigma}z_c\langle e^{-i\sqrt{2}\theta_\rho}\rangle\int_0^L dx\cos{[\sqrt{2}\theta_\rho(x)]}, \tag{39}$$

where z_c is the number of nearest neighbors in the transverse direction, L is the system size, and ρ_0 is the unperturbed density. We find a sine-Gordon-like Hamiltonian, and therefore, at $T < T_c$, $t_\perp$ opens a gap in the spectrum because the cosine wants to lock the field θ_ρ to one of the minima. In the thermodynamic limit, the zero-temperature gap Δ_ρ is known analytically [53]. This gap in the charge sector should equal the gap to the first excited state in Eq. (26), yet the notation is kept distinct due to the differing definitions of the gaps.

The dimensional crossover [37] that occurs in such systems is represented by the mean-field critical temperature T_c above which $\langle \psi_\uparrow^\dagger(x)\psi_\downarrow^\dagger(x)\rangle = 0$, and the system is made of incoherent and decoupled 1D chains [48]. This means that for $T > T_c$, the thermal fluctuations wash out the transverse coherence due to the presence of $t_\perp$. The system behaves essentially as if it was an isolated chain. Notably, the critical temperature scales like the charge gap at zero temperature; see Appendix F for more details. Even though the prefactors in both T_c and the charge gap are partially unknown, because of the constant C, the ratio is completely controlled by the Luttinger parameter K_ρ only which can be computed from numerical calculations (DMRG, Bethe ansatz, etc.),

$$R(K_\rho) = \frac{\Delta_\rho(T = 0)}{T_c} \tag{40}$$

$$= 2\pi \left[\frac{K_\rho \tan\left(\frac{\pi}{2}\frac{1}{4K_\rho - 1}\right)}{2\kappa^2(K_\rho/2)(4K_\rho - 1)\sin(\frac{\pi}{2K_\rho})B^2\left(\frac{1}{4K_\rho}, 1 - \frac{1}{2K_\rho}\right)} \right]^{\frac{K_\rho}{2K_\rho - 1}} \sin\left(\frac{\pi}{4K_\rho - 1}\right), \tag{41}$$

with $B(x, y)$ the Beta function and $\kappa(K)$ a combination of gamma functions $\Gamma(K)$ defined in Eq. (F6).

An exact extrapolation of the Luttinger parameter K_ρ can be reached via the Bethe ansatz solution [51]. A first successful attempt toward this direction for the XXZ model was given by Ref. [54]. Then, the 1D repulsive Hubbard correlation function exponents have been accessed directly [55]. It can be shown that a unitary transformation [56] allows us to map the problem from positive U to negative U (of our interest). By computing exactly the ground-state energy of the system, we extrapolate the charge stiffness and compressibility. A twist of the boundary condition gives the charge stiffness $\mathcal{D}_\rho(U < 0) = 2u_\rho K_\rho$, while the response to the number of particles corresponds to the charge compressibility $\chi_\rho(U < 0) = 2u_\rho/K_\rho$. Therefore, the parameter we inject in Eq. (40) is given by $K_\rho = \sqrt{\mathcal{D}_\rho/\chi_\rho}$ [57].

A more challenging case arises when $|U| \ll t$. Indeed, in that case, since $\Delta_\sigma \ll t$ the pairs are nonlocal, and the full bosonized form of the Hamiltonian with both charge and spin sectors [Eqs. (34) and (35)] must be used. To deal with this situation, we use a renormalization-group (RG) procedure (see Appendix G), in which we eliminate all degrees of freedom from the initial bandwidth of the system, down to the spin gap. At that scale, since the running ultraviolet cutoff is now identical to the spin gap, we are back to the situation where "local" pairs (hard-core bosons) hop in the transverse direction. The single-particle hopping thus disappears at that scale and simply leads to an effective Josephson coupling between the various 1D units. This coupling can be computed from the RG as detailed in Appendix G. The limit $\Delta_\sigma \ll W$, where $W \sim 2t$ is the bandwidth of the 1D system, corresponds naturally to the case of weak interactions $|U| \ll W$. In this regime, the spin gap either obtained from the Bethe ansatz for the Hubbard model, or more generally from the RG [58], is naturally exponentially small in the interactions $\Delta_\sigma \sim \sqrt{|U|}e^{-1/|U|}$. Thus, in order to be in the relevant regime, for the whole procedure to work, a very weak interchain hopping $t_\perp$ is needed. Specifically, the RG flow needs to be cut by the spin gap, and it may not be cut by the interchain hopping. If this condition is satisfied, we recover a model analogous to the one of the strong coupling albeit with a different Josephson parameter. As we discuss above, the ratio is insensitive to the precise value of the coupling, and thus, the ratio Eq. (40) is expected to hold for all values of U.

V. RESULTS

The primary focus of this section is to make use of and test the developed MPS + MF framework of the study case of negative-U Hubbard chain arrays. The methods described in Sec. II are tested thoroughly to produce a robust routine for determining critical temperature for the onset of superconductivity in Q1D systems of fermions with a gapped spin sector. These results are subsequently leveraged in Sec. VI to obtain T_c for USC in weakly coupled doped Hubbard ladders with repulsive interactions. The negative-U Hubbard chain array results are split into four subsections which are ordered as follows: (i) The Hamiltonian Eq. (18) depends on a range parameter of the mean fields which is studied in this subsection, (ii) a numerical study of the ground-state superconducting energy gap and critical temperature from thermal states, as well as (iii) comparing those numerical results with a more efficient mixture of analytics and numerics, and finally (iv) benchmarking MPS + MF against AFQMC in a 2D system where the latter approach yields quasiexact results.

As there are enough parameters to consider already, in the following results for chain arrays, we are targeting a fixed density

$$n = \frac{1}{L}\sum_i^L \sum_\sigma \langle c_{i,\sigma}^\dagger c_{i,\sigma} \rangle = 0.5, \tag{42}$$

i.e., a quarter-filled system. We expect other close-lying densities will not yield markedly different results due to the nature of the isotropic case having weak dependence on density around this filling in the 2D case [59].

A. Hamiltonian range dependence

Considering the effective 1D Hamiltonian of Eq. (18), the first question to be answered is how long range the mean-field terms can be. As we discuss at the end of Sec. II, the MF amplitudes will always decay with an exponential envelope as a function of the distance between the operators appearing in them. Since longer-range terms are more difficult to simulate, we want to find a minimal range for each parameter set with which longer-ranged Hamiltonians agree. As a metric for determining agreement, we use the order parameter and energy gap Δ: The former is defined by
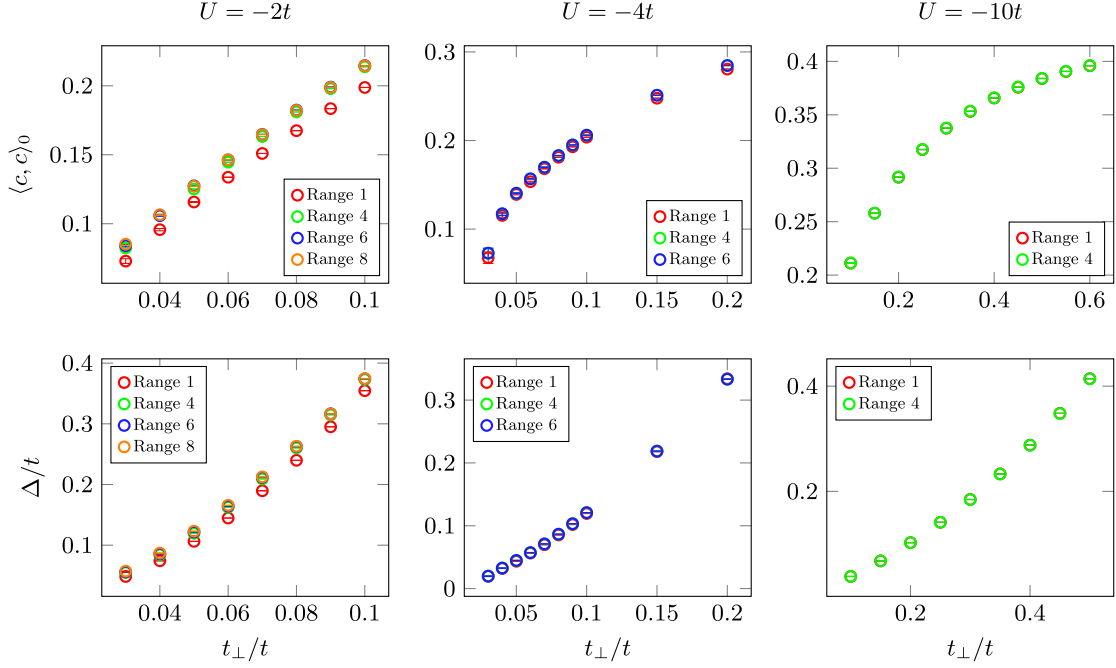
FIG. 10.   Range dependence of the order parameter defined in Eq. (43) and first excitation energy defined in Eq. (26) for different values of interaction $U/t = -2, -4, -10$ and density $n = 0.5$. Notably, the difference between the two largest ranges is not visible which indicates sufficient range in the Hamiltonian.

$$\langle c, c \rangle_r = \frac{1}{i_l - i_f + 1} \sum_{i=i_f}^{i_l} \langle c_{i,\uparrow} c_{i+r,\downarrow} \rangle, \qquad (43)$$

with $r = 0$ and where i_f and i_l are chosen to avoid boundary effects of the open-boundary conditions typical in DMRG. As can be seen from Fig. 10, the minimal range required varies with the strength of interaction. This is natural since weaker attraction makes electron pairs more dispersive and thus less localized.

We note that longer-ranged terms can still be finite and ignoring them should yield at the very least a difference in ground-state energies. However, the primary question is rather the degree at which these terms affect the ground-state wave function and the critical temperature. In Fig. 10, we show that the order parameter and excited-state gap Δ do not change appreciably beyond the ranges that are displayed. While we find α terms at longer ranges to be finite, Δ and the on-site order parameter are largely unaffected.

From the results in Fig. 10, we choose the range of pairing and particle-hole terms to use in the calculations. Notably, the same range is used for finite temperature as is used for ground-state calculations. We motivate this usage of range by considering the pairs formed prior to condensation. Such prior pair-forming is, in turn, motivated by a pairing strength larger than the critical temperature. For the interaction strengths studied at finite temperature, the pairing energy ends up at least twice the critical temperature and is equal to the spin gap in Table I. Such strong pairing motivates us to use the same range at both zero and finite temperature. Furthermore, the results of Fig. 10 can be used to motivate a range for ladder systems (see Sec. VI). These systems are close in behavior to weakly interacting attractive Hubbard chains. Since range is a costly parameter, we use $r = 3$ which is the smallest range that can feasibly be considered having small difference with longer ranges as seen in Fig. 10. This will improve run times while affecting critical temperature adversely.

B. Numerical results

Using the minimal ranges, we may compute the ground and finite-temperature states for the Hamiltonian Eq. (18) using the MPS + MF framework. As shown in Fig. 11(a), we find the critical temperature decreasing with transverse tunneling $t_\perp$, vanishing as expected for $t_\perp \to 0$.

The excited-state gap Δ disappears in the same manner. Notably, the zero-temperature gap in field theory Δ_ρ should have the same meaning as the excited-state gap Δ, which is verified. Thus, from field theory it is expected that both T_c and Δ scale with $t_\perp$ with the same exponent, as can be seen from Eqs. (F4) and (F5).

In determining T_c numerically via state purification within the MPS approach, we have to contend with the increase in inverse temperature $\beta = 1/T$ required as $t_\perp$ is decreased. This results not just in longer imaginary-time evolutions, but also in increased finite-size effects (see Appendix A).

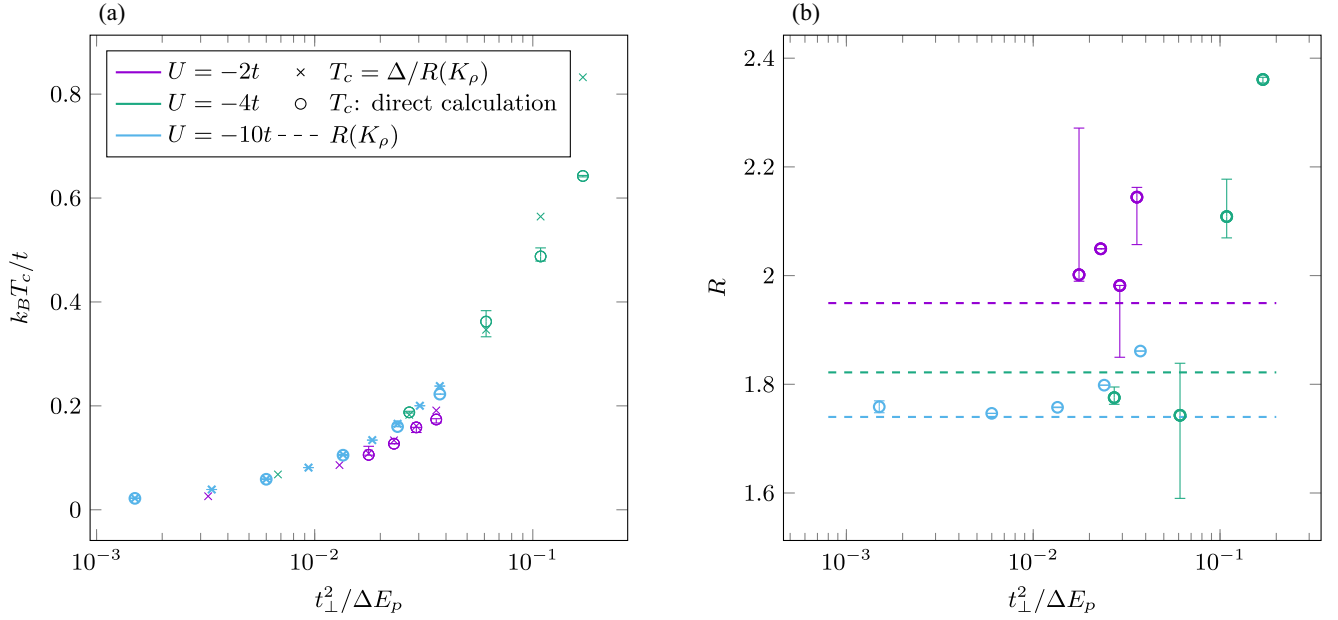Reaching large system sizes for these thermal-state calculations can be challenging. We use two different

FIG. 11. A comparison of analytical methods and combination with numerical methods for several values of interaction. Panel (a) shows critical temperature T_c vs transverse tunneling $t_\perp^2/\Delta E_p$. Circles show data obtained via direct calculation of thermal states, while crosses show T_c computed from zero-temperature calculations using the excitation gap Δ and Eq. (40). Panel (b) shows the ratio $R = \Delta/T_c$ of ground-state excitation gap to critical temperature, both computed separately, compared with the analytical ratio Eq. (40) (dashed lines) vs $t_\perp^2/\Delta E_p$.

approaches. In the first, used for $U = -10t$, the infinite-temperature purified starting state of the imaginary-time evolution is constructed to be in the $S = 0$ subspace, which allows us to keep exploiting the conserved spin quantum number during the evolution. The drawback is that this $\beta = 0$ initial state has entanglement growing strongly with system size, limiting the practically attainable system lengths.

The second approach, employed for $U = -2t, -4t$, is to sacrifice the spin conservation. This makes the purified initial state into a trivial-to-construct product state, and thus arbitrary system lengths are accessible. However, this makes the imaginary-time evolution more costly, as there are no conserved quantum numbers anymore. In order to alleviate this issue, we use the projected-purified (PP)-DMRG framework [60] expounded upon in Appendix B. We moreover rely on the ability of H_{MF} to filter out the $S=0$ subspace at temperatures at and below T_c. We ascertain this to be correct, with violations of $\langle S_z \rangle = 0$ reaching at most 10^{-2}, and typically much less, across all calculations.

C. Numerical-analytical hybrid results

For the field theory of Sec. IV, it is difficult to quantify the superconducting T_c or the excited-state gap Δ, due to the unknown prefactors arising from the massive spin sector. However, forming the ratio $\Delta/T_c = R(K_\rho)$ is free from these unknown prefactors, depending just on the TLL parameter K_ρ (computed in Table I) and is, strikingly, constant in $t_\perp$.

Generating R from the numerically determined data of Fig. 11(a) and the analytical expression Eq. (40) yields Fig. 11(b). Notably, while the analytical ratio is not agreeing with numerical estimates exactly, the constant nature of the analytics is likely approximative. Achieving a ratio which lies close enough to the data is sufficient in order to obtain critical temperatures. With this knowledge, the new T_c estimate becomes

$$T_c = \frac{\Delta(T = 0)}{R(K_\rho)}. \tag{44}$$

Since the primary issues of the T_c computation come from the imaginary-time evolution, we may now obtain T_c estimates from ground-state DMRG by computing $\Delta(T = 0)$. As shown in Fig. 11(a), the estimation scheme Eq. (44) is agreeing very well with the numerical T_c values obtained from thermal-state calculations.

TABLE I. Results from the Bethe ansatz solution of the 1D Hubbard model with attractive interaction at quarter filling. Here, we compute the TLL parameter of charge sector K_ρ and the field theory spin gap Δ_σ as a function of the interactions.

U/t	K_ρ	Δ_σ/t
−2.0	1.26	0.289
−4.0	1.41	1.476
−10.0	1.51	6.671

Since the more efficient ground-state DMRG is the main tool of this alternative way to obtain T_c, it can be brought to even lower values of $t_\perp$ and greater system sizes, allowing for greater precision at larger parameter ranges.

D. Comparison with AFQMC

In Eq. (18), the coordination number z_c tracks the dimensionality of the underlying Q1D array. For the calculations on 3D Q1D systems, as performed so far, we have $z_c = 4$. Lattices of other dimension can be simulated just as well, just by changing z_c to the appropriate value.

We exploit this for benchmarking the MPS + MF approach against quasiexact results, which AFQMC is able to obtain in the absence of a sign problem. These benchmarks are necessarily done for 2D models, as the finite-temperature algorithm uses scales cubically in the number of lattice sites [41,42]. We stress that the MPS + MF method describes ordering in the Ginzburg-Landau sense via the pairing mean fields α_{ik}, while AFQMC detects the actual 2D Berezinskii-Kosterlitz-Thouless (BKT) transition. We interpret the mean-field T_c of MPS + MF as an approximation of the T_{BKT} which occurs for the 2D model.

We compare the two algorithms both for ground-state and finite-temperature calculations. For ground states, which do achieve superconducting long-range order even in 2D, the on-site order parameter is compared to the two algorithms as shown in Fig. 12(a). Since 2D is the lower critical dimension, quantum fluctuations around any mean will be especially strong. Considering this fact, we note that the smallest simulated $t_\perp$ values have a modest overestimation as MPS + MF neglects transverse quantum fluctuations by design.

For finite-temperature states, we compute the BKT transition temperature T_{BKT} using AFQMC and compare it to T_c from MPS + MF. The strategy for obtaining the T_{BKT} temperature from AFQMC is standard and elaborated in Appendix D. Both T_{BKT} and T_c, as well as their ratio, are shown in Fig. 12(b). Over the range of $t_\perp$ for which we simulate, the near-constant ratio between T_c and T_{BKT} is striking, being approximately

$$\frac{T_{BKT}}{T_c} \approx 0.25. \qquad (45)$$

This is in line with previous work where we also found such a ratio to be robust to changes in parameters [37]. Similar to the comparison to zero-temperature AFQMC, MPS + MF will overestimate the transition due to the neglect of both quantum and thermal fluctuations, and these will again be especially pronounced, given that these are 2D systems. Previous work on bosonic systems, as well as the generally known dependence of phase transitions on spatial dimensionality of a system, indicates that these fluctuations will be strongly reduced for a Q1D 3D system [37].
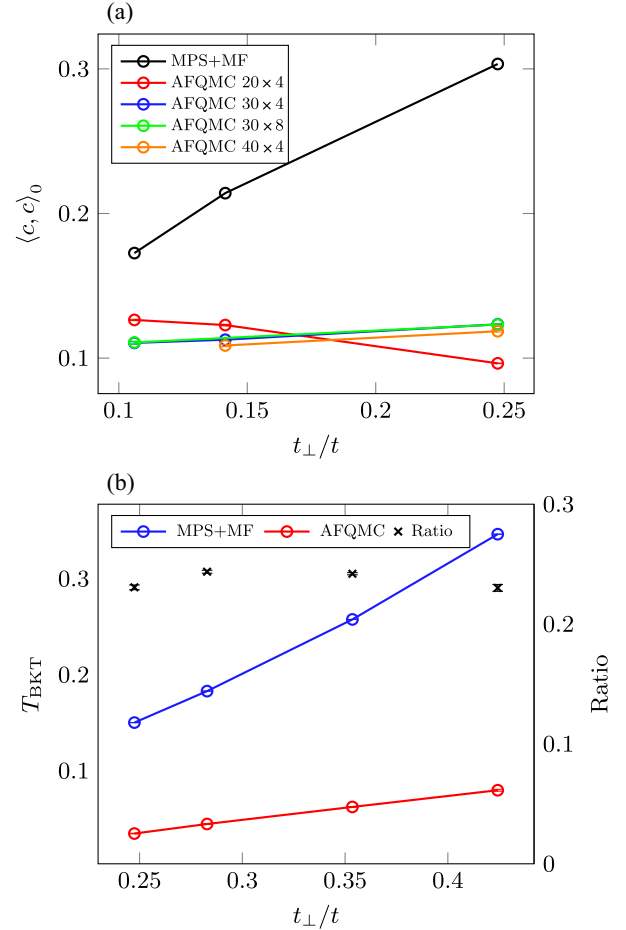

FIG. 12. Comparison of AFQMC and MPS + MF for (a) ground-state order parameter at $U = -2t$, $n = 0.5$ and (b) T_c from MPS + MF and T_{BKT} from AFQMC at $U = -4t$ and $n = 0.5$. Black crosses denote the ratio T_{BKT}/T_c.

Specifically, there we found that $T_c^{QMC}/T_c^{MPS+MF} \approx 0.7$. For 3D fermionic Q1D systems, we thus expect that a correction factor for T_c computed from the MPS + MF framework to obtain the true T_c will lie somewhere between these two extremes, and probably closer to 0.7 than to 0.25.

VI. 3D ARRAY OF WEAKLY DOPED REPULSIVE-U HUBBARD LADDER

With the MPS + MF framework for fermions developed on 3D Q1D systems of negative-U Hubbard chains, this section applies it to a much more demanding system: 3D arrays of weakly coupled, doped, repulsive-U Hubbard ladders. These systems have been investigated via field theory as an alternative to Q2D systems in the study of USC and high-T_c superconductivity. The microscopic mechanism of repulsively mediated pairing is understood from field theory, and the strength of this pairing can be quantified reliably via MPS-based methods. Despite these

critical advantages over the Q2D models, there was no quantitative method to study these 3D arrays that incorporates the pairing physics at the microscopic level, as the TLL field theory in practice yields largely qualitative results.

The MPS + MF framework supplies that ability. Just like the negative-U Hubbard chains, the isolated, doped, repulsive-U Hubbard ladders have finite ΔE_s and ΔE_p, manifesting the repulsively mediated pairing. Further, when analyzed via renormalization-group theory within the TLL approach, the low-energy physics of both these 1D subunits is structurally analogous. Both exhibit an ungapped charge sector characterized by a TLL coefficient K_ρ for the chain, and $K_{\rho,+}$ for the ladder. Furthermore, both can be computed from the microscopic Hamiltonians via MPS methods. For the Hubbard ladders, there are three additional gapped modes, a charge one and two spin ones, the smaller having minimal energy ΔE_s, as for the single-spin mode in the negative-U chains.

The MPS + MF framework can thus be applied to the Hubbard-ladder arrays. For a proof-of-principle treatment, we focus on plain Hubbard ladders depicted in Fig. 1(b), with $U = 8t$ and average density fixed at $n = 0.9375$. The characteristic energy scales and TLL parameters can be computed with DMRG which results in $\Delta E_s \approx 0.078t$, $\Delta E_p \approx 0.134t$, and $K_{\rho,+} = 0.77$ (the TLL parameter extracted from Ref. [6]). The study of optimized Hubbard-ladder arrays engineered for high T_c's via deliberate optimization of ΔE_s, ΔE_p, and K_ρ, as well as examining the possibility of charge-density order competing with USC within two-channel MPS + MF, is the subject of forthcoming future work.

As ladder geometries require much larger MPS resources than chains, direct calculation of T_c, while feasible, is challenging. We thus use MPS + MF combined with the analytics developed and tested in Secs. II–V. In this manner, we obtain T_c for USC in these arrays by computing excited-state energy gaps Δ using DMRG for ground states, then applying Eq. (44). Compared to Secs. IV and V, this procedure requires only marginal adjustments for the ladder as the negative-U chain and Hubbard ladder look largely identical in the low-energy parts of their respective field theories. For the former system, the order parameter scales as $e^{-i\sqrt{2}\theta_\rho(x)}$ in the phase operator of the ungapped charge mode, while for the latter it is $e^{-i\theta_{\rho,+}(x)}$. From that, it follows that the ratio function for the ladder is

$$R_{\text{ladder}}(K_{\rho,+}) = R(2K_{\rho,+}), \qquad (46)$$

where R is given by Eq. (40). Thus, R_{ladder} will retain its dependence on a single TLL parameter: $K_{\rho,+}$. This is due to the gapped spin sectors entering the order parameter in the same manner both for T_c and Δ. These nonuniversal contributions thus cancel when forming R, analogous to the derivation in Sec. IV and Appendix F. The same analysis yields that for the ladder we have

$$T_c \propto t_\perp^{\frac{4K_{\rho,+}}{4K_{\rho,+}-1}}. \qquad (47)$$

The effective MF Hamiltonian for the Q1D array of the ladders is given by

$$H_{\text{HL}} = -t \sum_{i=1}^{L-1} \sum_{j=0}^{1} \sum_\sigma (c_{i+1,j,\sigma}^\dagger c_{i,j,\sigma} + c_{i,j,\sigma}^\dagger c_{i+1,j,\sigma}) - t \sum_{i=1}^{L} \sum_\sigma (c_{i,1,\sigma}^\dagger c_{i,0,\sigma} + c_{i,0,\sigma}^\dagger c_{i,1,\sigma})$$
$$- \mu \sum_{i,j} n_{i,j} + U \sum_{i,j} n_{i,j,\uparrow} n_{i,j,\downarrow} - H_{\text{pair,MF}} - H_{\text{exc,MF}}, \qquad (48)$$

where i, j are leg and rung indices, respectively, and $H_{\text{pair,MF}}$ and $H_{\text{exc,MF}}$ are derived in Appendix E and defined by

$$H_{\text{pair,MF}} = \sum_{i,i',j,j'} \alpha_{i,i',j,j'}(c_{i,j,\downarrow}^\dagger c_{i',j',\uparrow}^\dagger + c_{i',j',\uparrow} c_{i,j,\downarrow}), \quad (49)$$

$$H_{\text{exc,MF}} = -\sum_{i,i',j,j',\sigma} \beta_{i,i',j,j',\sigma} c_{i,j,\sigma}^\dagger c_{i',j',\sigma}, \qquad (50)$$

and the pairing amplitudes are given by

$$\alpha_{i,i',0,0} = \frac{2t_\perp^2}{\Delta E_p}(\langle c_{i',1,\uparrow} c_{i,1,\downarrow}\rangle + 2\langle c_{i',0,\uparrow} c_{i,0,\downarrow}\rangle), \quad (51)$$

$$\alpha_{i,i',1,1} = \frac{2t_\perp^2}{\Delta E_p}(\langle c_{i',0,\uparrow} c_{i,0,\downarrow}\rangle + 2\langle c_{i',1,\uparrow} c_{i,1,\downarrow}\rangle), \quad (52)$$

$$\alpha_{i,i',1,0} = \frac{4t_\perp^2}{\Delta E_p}\langle c_{i',0,\uparrow} c_{i,1,\downarrow}\rangle, \qquad (53)$$

$$\alpha_{i,i',0,1} = \frac{4t_\perp^2}{\Delta E_p}\langle c_{i',1,\uparrow} c_{i,0,\downarrow}\rangle, \qquad (54)$$

whereas the exchange terms are given by

$$\beta_{i,i',0,0,\sigma} = \frac{2t_\perp^2}{\Delta E_p}(\langle c_{i,1,\sigma}^\dagger c_{i',1,\sigma}\rangle + 2\langle c_{i,0,\sigma}^\dagger c_{i',0,\sigma}\rangle), \quad (55)$$

$$\beta_{i,i',1,1,\sigma} = \frac{2t_\perp^2}{\Delta E_p}(\langle c_{i,0,\sigma}^\dagger c_{i',0,\sigma}\rangle + 2\langle c_{i,1,\sigma}^\dagger c_{i',1,\sigma}\rangle), \quad (56)$$

$$\beta_{i,i',1,0,\sigma} = \frac{4t_\perp^2}{\Delta E_p}\langle c_{i',0,\sigma}^\dagger c_{i,1,\sigma}\rangle, \quad (57)$$

$$\beta_{i,i',0,1,\sigma} = \frac{4t_\perp^2}{\Delta E_p}\langle c_{i',1,\sigma}^\dagger c_{i,0,\sigma}\rangle. \quad (58)$$

In this work, we exclude the possibility for a CDW phase such that density is independent of which rung we measure and is constant throughout the system. This is obtained by the restriction $\beta_{i_1,i_1,j_1,j_1,\sigma} = \beta_{i_2,i_2,j_1,j_1,\sigma}$. We note that inclusion of the exchange terms $\beta_{i,i',l,l',\sigma}$ has previously not been possible by analytical methods.

In isolation, Hubbard ladders typically require large bond dimensions for accurate simulations (see, e.g., Ref. [6]). With the included superconducting MF ordering channel, we find this requirement to be relaxed. This is expected, as any long-range order, be it in real space or momentum space, requires fewer retained Schmidt components than for that same system without such an order. However, at these lowered bond dimensions, converged MF amplitudes exhibit non-negligible dependence on the bond dimension despite modest truncation errors. Regardless of this, the linear scaling of energy with truncation error, typically found in DMRG, remains intact even here as shown in Fig. 13(a)–13(c). We note that while we always find $E_0(\chi) < E_1(\chi)$, as has to be the case, the lines interpolating in truncated weight ϵ_ψ down to zero may cross, giving the appearance of level crossing. However,
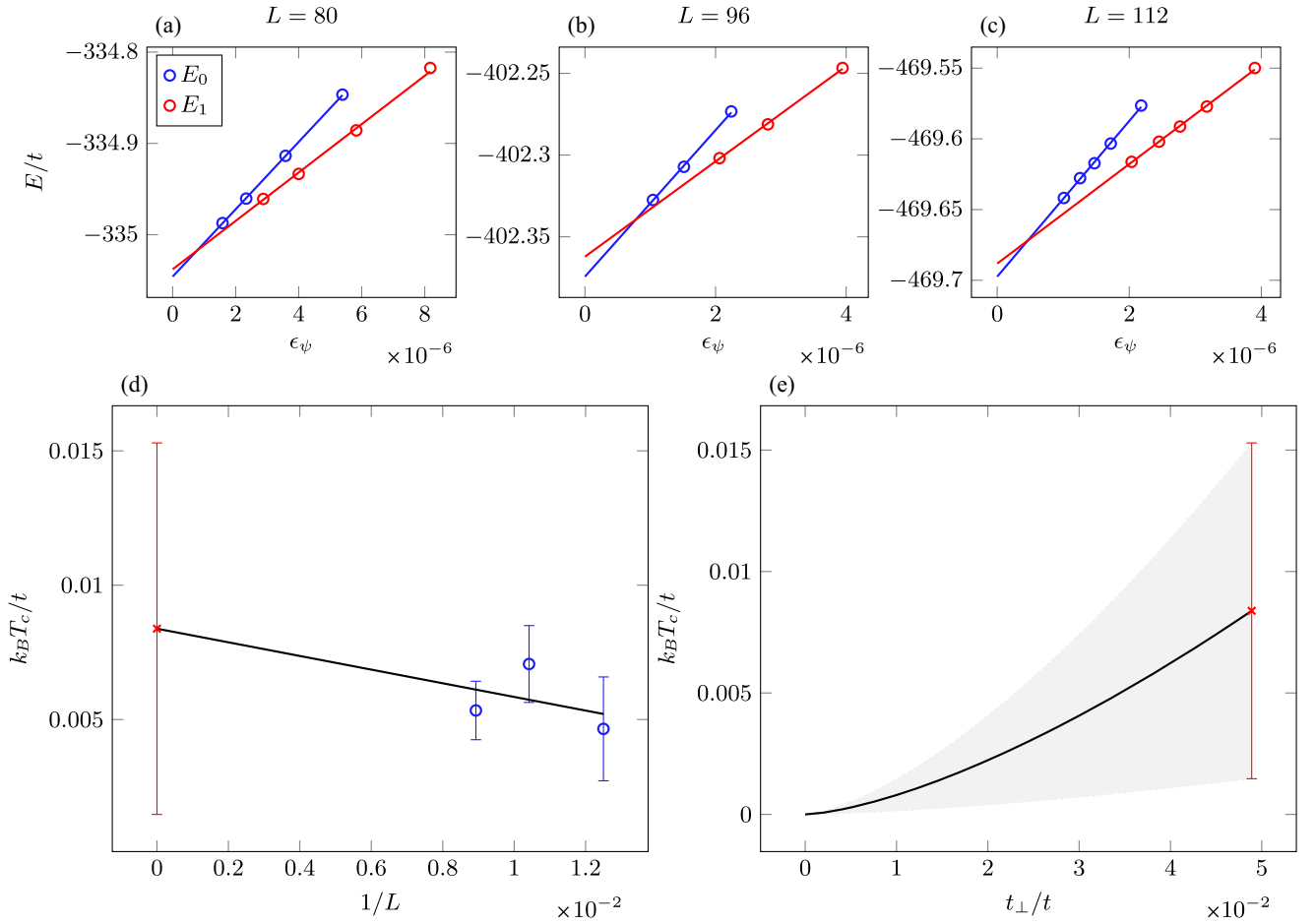

FIG. 13. Energy gap to the first excited state and critical temperature of the Hubbard ladder for $U = 8t$, $n = 0.9375$, $t_\perp = 0.0489t$, and MF terms with range $r = 3$. The panels show ground-state energy E_0 (blue circles) and excited-state energy E_1 (red circles) plotted against their truncation error ϵ_ψ and extrapolated to zero truncation error (blue and red lines) for a ladder with length (a) $L = 80$, (b) $L = 96$, (c) $L = 112$. While $E_1(\epsilon_\psi) > E_0(\epsilon_\psi)$ can happen, this comparison is meaningless, as only energies at the same χ can be compared (cf. main text), where we always find $E_0(\chi) < E_1(\chi)$. Continuing, (d) shows the critical temperature of the 3D ladder array $T_c = \Delta/R_{\text{ladder}}(K_{\rho,+}) = [E_1 - E_0/R_{\text{ladder}}(K_{\rho,+})]$ extrapolated to infinite size where $R_{\text{ladder}}(K_{\rho,+})$ is given by Eq. (46) and $K_{\rho,+} = 0.77$ [6], while (e) shows the critical temperature vs $t_\perp$ exploiting the scaling known from Eq. (F4), using the T_c value obtained in (d) (red cross).

only energies at the same χ can be directly compared as each value of χ corresponds to a separate optimization problem in the MPS approach, with distinct effective Hamiltonians. Thus, it is possible to compute the mean-field amplitudes at modest bond dimension and obtain energy measurements, and thus Δ extrapolated to zero truncation error at different system sizes.

Finally, we obtain Δ, and thus T_c after rescaling with Eq. (46), in the thermodynamic regime via infinite-size extrapolation as shown in Fig. 13(d). We note that $t_\perp$ is chosen quite close to ΔE_p and ΔE_s. The primary reason is the small energy gaps we need to resolve. At smaller values of $t_\perp$, the discrete energy gaps of the finite-length systems mask Δ even for ladders with $L = 80$ or even larger. However, using Eq. (47) it is possible to extrapolate thermodynamic T_c to smaller, physically more reasonable values of $t_\perp$ as shown in Fig. 13(e).

VII. RESOURCE REQUIREMENTS

In this section, we summarize time and resource consumption for the different algorithms used in this work. The MPS + MF routines feature repeated DMRG solutions. Generally, the total number of CPU-core hours τ scales with the same parameters as DMRG does, i.e.,

$$\tau_{\mathrm{MPS}} \sim L d^2 \chi^3, \tag{59}$$

where L is the number of lattice sites (and thus, MPS tensors), d the size of the local Hilbert space, and χ is bond dimension. The number of loops required to reach self-consistency N_{tot} is shown for representative examples in Fig. 5 and subject to the optimizations mentioned in Sec. III C. The total resources consumed by the algorithm are thus given by

$$\tau_{\mathrm{MPS+MF}} \sim N_{\mathrm{tot}} \tau_{\mathrm{MPS}}. \tag{60}$$

For the ground states of the negative-U Hubbard chain with MF amplitudes, we use MPS-based DMRG from the Matrix Product Toolkit package [61]. The data are computed using Intel Xeon E5 2630 v4 at 2.20-GHz CPU cores. Most results are obtained at a bond dimension of $\chi = 300$. A certain speedup is obtained using two CPU cores and threads used in the LAPACK and BLAS routines on which the algorithm rests. For a typical run, a single MF loop takes about 8000s of wall-clock time for $\chi = 300$ and $L = 100$. Notably $d = 4$ for the negative-U Hubbard chain. With two CPU cores in use for this calculation, the total required resources for solution are $\tau_{\mathrm{MPS+MF}} \approx 5 N_{\mathrm{tot}}$ CPU-core hours.

Additionally, in order to obtain critical temperatures directly, we calculate thermal states using imaginary-time evolution of purified states. For simpler Hamiltonians where a shorter range (maximum of 1) for both $\alpha_{i,k}$ and $\beta_{i,r,\sigma}$ is possible, Trotterized time evolution suffices

[32,45]. For this case, we use a time step of $\delta\tau = 0.1$ and a fourth-order Trotter discretization. With additional linear scaling in the length of the imaginary time simulated (equal to half the inverse temperature β), a typical solution requires about 12 000s of wall-clock time for $L = 60$, $\chi = 200$, and $\beta = 9.5$. Having used two CPU cores, the required resources in total are $\tau_{\mathrm{MPS+MF}} \approx 7 N_{\mathrm{tot}}$ CPU-core hours. Notably, the range of inverse temperature β to be simulated to determine T_c changes markedly with $t_\perp$, leading to commensurate changes in τ.

In the case of Hamiltonians with long-range terms, it is necessary to apply more advanced time-evolution schemes. With that, the resource requirements increase significantly; i.e., a typical solution requires about 32 000s on six CPU cores for $L = 60$, $\beta = 9.5$, and $\chi = 100$, leading to an overall $\tau_{\mathrm{MPS+MF}} \approx 53 N_{\mathrm{tot}}$ CPU-core hours. In part, this increase is due to the longer-range couplings. Another cause is the increased effective system size. This increase, in turn, is down to the specific MPS implementation [62] used, which always requires full quantum number conservation. In our use case, where both charge and spin conservation are discarded (cf. Sec. V B), quantum numbers are restored artificially via the use of PP-DMRG [60] at the price of a larger effective system. Further details on obtaining finite-temperature results are provided in the Appendixes A and B.

Exact ground-state order parameters in finite lattices are computed with an AFQMC method using generalized METROPOLIS with force bias [63]. This algorithm scales quadratically with the number of electrons N_e and linearly with the number of lattice sites N_l:

$$\tau_{\mathrm{AFQMC,GS}} \sim N_l N_e^2. \tag{61}$$

For an $N_l = 40 \times 4 = 160$ system with 80 electrons, we perform calculations of 2000 sweeps for measurements after ten sweeps of thermalization, with 100 independent repeats. Such a calculation, with an imaginary propagation time β set to 64, takes 49 hours of wall-clock time on 100 Intel Xeon E5-2640 v4 2.4-GHz cores yielding a requirement of $\tau_{\mathrm{AFQMC,GS}} \approx 4900$ CPU-core hours.

In order to obtain exact values for T_{BKT} in two-dimensional Q1D as a benchmark for MPS + MF (cf. Sec. V D), we use finite-temperature AFQMC. The package utilized for this purpose is called Algorithms for Lattice Fermions (ALF) [41,42]. Data are obtained with an algorithm which scales cubically in the number of lattice sites N and linearly with inverse temperature β:

$$\tau_{\mathrm{AFQMC}} \sim \beta N^3. \tag{62}$$

An improvement of this scaling is available [64], but it is not implemented for our calculations. We find that a single instance of sampling requires approximately 200s for $N = 48 \times 8 = 384$ and $\beta = 20$ using an Intel Xeon E5-2698 v3

2.30-GHz CPU core. Statistical error bars are sufficiently small for a sample size of approximately 100 000 for the parameter set we study, requiring $\tau_{\text{AFQMC}} \approx 5000$ CPU-core hours. The ALF package, like most QMC implementations, can of course parallelize this workload near perfectly.

When performing MPS + MF on the weakly coupled repulsive-U Hubbard ladders, MPS + MF becomes more resource intensive: As earlier, one conserved quantum number is lost, and the matrix product operator representing the Hamiltonian is significantly larger than any for the negative-U Hubbard chains. We use a DMRG implementation offering distributed-memory parallelism (pDMRG) to obtain faster solutions [14]. Different from QMC-type algorithms, any such parallelization will inevitably show nontrivial communication overheads, and thus not scale linearly in the number of MPI processes. For a single converged ground state from pDMRG, we thus require approximately 27 000s using $32 \times 8 = 256$ Intel Xeon E5-2698 v3 2.30-GHz CPU cores, at $\chi = 1000$ and $L = 96$. The total cost thus becomes $\tau \approx 2000 N_{\text{tot}}$ CPU-core hours. The optimizations of Sec. III C particularly apply to the Hubbard-ladder systems. Without these optimizations, N_{tot} can be as high as $N_{\text{tot}} = 25$, but by employing them, where possible, it can drop as low as $N_{\text{tot}} = 6$.

VIII. CONCLUSION

In this work, we develop a numerical framework combining MPS-based numerics with MF and perturbation theory to solve correlated quasi-one-dimensional fermionic systems constructed out of weakly coupled 1D subunits, in two and three spatial dimensions. This method relies on MF-approximating tunneling processes occurring transverse to the 1D subunits with amplitude $t_\perp$. The requirement for this approximation being reasonable is that $t_\perp$ be weaker than any gap on the 1D subunits that suppress first-order tunneling between 1D subunits. Using the example of superconductivity in such Q1D arrays, we show how this framework allows us to map otherwise difficult or even intractable correlated-fermion models in 2D and 3D onto a self-consistent 1D problem. We then demonstrate how these can be effectively solved both for ground states and thermal states.

We test the framework on a model of attractive fermions on a 1D chain extensively comparing to both analytical methods and AFQMC. We obtain analytical expressions for superconducting T_c of the model and the gap Δ to the first excited state. Utilizing that a ratio $R = \Delta/T_c$ of these two quantities remains constant over $t_\perp$, we obtain R analytically and greatly speed up the calculation of T_c via the use of Δ and R. Comparing this value with T_c obtained directly from thermal-state calculations shows that obtaining T_c from Δ and R yields excellent agreement, especially at small $t_\perp$. This allows MPS + MF to obtain T_c without using imaginary-time evolution, which is numerically more costly than obtaining Δ via ground-state calculations.

Subsequently, we use the gap and ratio method to obtain T_c from MPS + MF and compare with T_{BKT} from AFQMC. We find a semiconstant ratio of these temperatures over a range of $t_\perp$, in line with previous comparisons to QMC [37]. As expected, the MF approximation yields greater overestimation of the ordering temperature for lower-dimensional systems. With this in mind, the method seems able to provide reliable estimates of T_c in fermionic systems for an appropriate choice of parameters.

Utilizing the developed MPS + MF framework, we treat the case of a 3D array of weakly coupled, doped Hubbard ladders with strong repulsive interaction. With the tools developed in this work, we are able to calculate T_c quantitatively for the first time for these systems. The MPS + MF framework thus allows the efficient simulation of a subgroup of 3D systems of strongly correlated fermions, namely, the Q1D models, which have been very challenging to address for any quantitative method.

Notably, the 3D arrays of weakly coupled Hubbard ladders studied in this work have not been optimized to yield large critical temperatures. Previous work has indicated that by modifying the ladder parameters, larger T_c's may be achieved [5]. With the MPS + MF framework, it is possible to systematically search for improved critical temperatures starting from the microscopic models. This allows us to not only deliberately search for optimal high-T_c prototype materials in the Q1D space, something that remains elusive for Q2D materials, but it likewise permits us to design ultracold-gas experiments capable of observing analog states of high-T_c superconductivity within current or near-future experimental constraints. We are pursuing both possibilities in current follow-up work.

In this work, we focus on the physics of superconductivity using the MPS + MF routine. However, MPS + MF can be used for any Q1D system in which tunneling in between 1D subunits is suppressed at first order by a gap. This gap can be of any physical nature, such as, e.g., the charge gap present in the insulating phases of the Bechgaard and Fabre salts. The MPS + MF framework can thus also be deployed to understand, e.g., the antiferromagnet to spin-density wave transition in these materials. This potential application of the framework highlights its power to incorporate multiple ordering channels simultaneously at the mean-field level, and thus its ability to resolve the competition between competing orders.

Finally, the capacity of MPS numerics to address real-time dynamics of many-body systems both near and far from equilibrium opens the possibility to use the MPS + MF algorithm to study real-time dynamics of correlated fermions in high-dimensional Q1D systems. Such forthcoming work is currently in preparation on dynamically induced superconductivity in such systems [43].

ACKNOWLEDGMENTS

APPENDIX A: FINITE-SIZE EXTRAPOLATION

The Q1D models we consider in this paper suffer from finite-size effects like all numerics on finite systems. In particular, as the connection between 1D systems weakens, so does the strength of the resulting superconductor resulting in increased healing lengths. Additionally, we find that finite-size effects persist even at large $t_\perp$ albeit reduced in size. In order to accurately simulate these systems, extrapolation has to be performed on the finite-size observables to the limit of infinite size.

Using MPS numerics, we compute the observables to be measured for several system sizes. We then utilize various strategies to obtain infinite-size values depending on the type of finite-size effect and observable. The strategies are outlined in this appendix.

1. Local observables

For local quantities such as the order parameter and energy, we use a common heuristic

$$O(L) = O_\infty + c_0 \frac{1}{L} + c_1 \frac{1}{L^2} + \mathcal{O}(L^{-3}), \qquad \text{(A1)}$$

where $O(L)$ is a measurement of any local observable for a system size L and O_∞ the thermodynamic limit of that observable. Thus, we fit measurements at finite size to a quadratic polynomial in inverse size. We find that the data fit the heuristic pretty well as shown in Fig. 14.

2. Finite temperature at criticality

Several results in this work obtain the critical temperature of a system by evolving in imaginary time. The phase transition point is dependent on system size. For the case of significant finite-size effects, we consider the
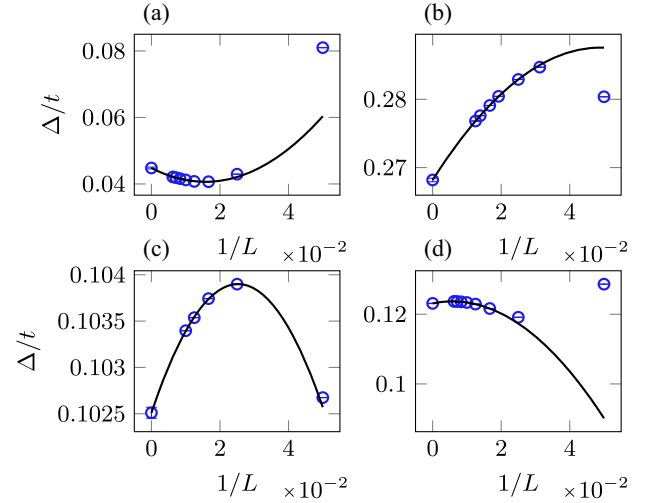

FIG. 14. Examples of finite-size extrapolations of the gap from the ground state to the first excited state (Δ) for (a) $t_\perp = 0.05t$, $U = -4t$, (b) $t_\perp = 0.175t$, $U = -4t$, (c) $t_\perp = 0.2t$, $U = -10t$, and (d) $t_\perp = 0.05t$, $U = -2t$. All data at $n = 0.5$.

critical behavior of the superconducting order parameter in particular, as that determines when the system enters superconductivity.

a. Significant finite-size effects

When finite-size effects must be considered, we follow a common strategy used, e.g., on QMC results [65] called data collapse. We study a second-order phase transition, where the critical behavior of the order parameter (here named ψ for simpler notation) is given by

$$\psi_L(t) = L^{-\beta/\nu} \tilde{\psi}(L^{-1/\nu} t). \qquad \text{(A2)}$$

The reduced temperature t is given by

$$t = \frac{T - T_c}{T_c}, \qquad \text{(A3)}$$

and critical exponents β, ν are given by

$$\psi \sim |t|^\beta, \qquad \text{(A4)}$$

$$\xi \sim |t|^\nu, \qquad \text{(A5)}$$

where ξ is the correlation length of the ordering field. Notably, on the unordered side the order parameter is zero. In order to extract T_c we assume that our system's critical behavior belongs to the mean-field universality class which is consistent with fits to Eq. (A4) close to transition such that $\beta = \nu = 0.5$. Using these exponents, the finite-size order parameter is rescaled by $L^{\beta/\nu}$ and plotted over $L^{1/\nu} t$,

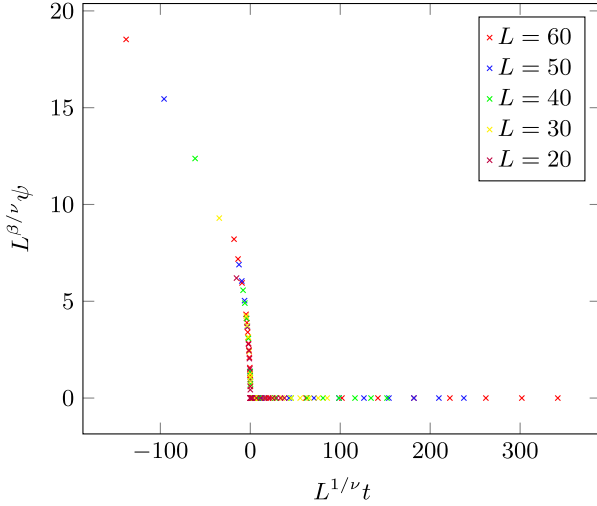$$\tilde{\psi}(x) = L^{\beta/\nu} \psi_L(L^{-1/\nu} x). \qquad \text{(A6)}$$

FIG. 15. The rescaled order parameter plotted against reduced temperature $t = (T - T_c/T_c)$ for $U = -10t$, $t_\perp = 0.3t$, and $n = 0.5$. The critical temperature is obtained by minimizing Eq. (A7).

The function $\tilde{\psi}(x)$ is the scaling function of the order parameter and is system size independent. Thus, for a correct choice of T_c all curves overlap close to transition as shown in Fig. 15. The quality of the collapse is determined using

$$s_\psi^2 = \frac{1}{x_{\max} - x_{\min}}$$
$$\times \int_{x_{\min}}^{x_{\max}} \frac{\sum_L \tilde{\psi}_L(x)^2}{N} - \left[\frac{\sum_L \tilde{\psi}_L(x)}{N}\right]^2 dx, \qquad \text{(A7)}$$

where N is the number of system sizes, s_ψ^2 is the variance integrated over a range $[x_{\min}, x_{\max}]$, and $\tilde{\psi}_L(x)$ is the scaling function for size L given a T_c. The range is chosen to lie around the proposed value of T_c. The critical temperature is then obtained for different widths Δx of the integration interval, and the resulting critical temperature is extrapolated to its value at zero width. The final error bar shown in values for T_c is taken to be the fitting error for decreasing width Δx. This treatment ultimately gives a small error bar. Added data for larger sizes might move the result outside this error bar.

For parameter sets where $t_\perp$ is particularly small, generating data close to transition is tricky due to slow convergence of the mean-field amplitudes. One consequence of this is that the data used for collapse can end up too far from transition for finite-size scaling to apply. On such an occasion, the analysis fails to produce reliable collapse of data and another strategy is needed.

b. Critical temperature interval

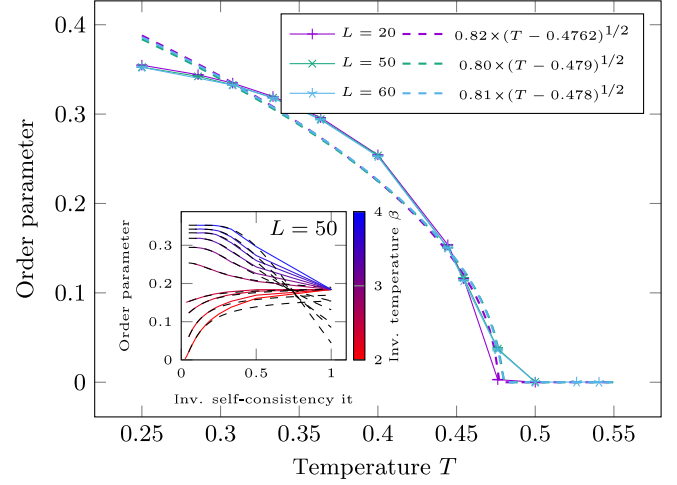When the previous analysis fails to produce a reasonable collapse, we generate a grid around the estimated phase

FIG. 16. Example obtaining T_c from fits without finite-size scaling for $U = -4t$, $t_\perp = 0.4t$, $n = 0.5$. Symbols denote the on-site order parameter extrapolated to infinite number of iterations for $L = 20$ (plus), $L = 50$ (cross), and $L = 60$ (star) computed via MPS $+$ MF for thermal states. Solid lines are guides to the eye. Dashed lines are fits with ansatz Eq. (A8). Inset shows an example of extrapolating the order parameter to infinite numbers of iterations for $L = 50$.

transition. Since the convergence close to the phase transition is especially demanding, we focus on surrounding temperatures. In order to reduce the number of necessary self-consistency iterations, we extrapolate the order parameter via $O(n) = O_{n\to\infty} + a \times \exp(-bn)$ in the number of self-consistency iterations n. Those extrapolations are shown as an example in the inset of Fig. 16 for $L = 50$, but for convenience, they are plotted over the inverse number of iterations. The results of these extrapolations are then used within to fit the data with

$$O(T) = \begin{cases} a|T - T_c|^{\frac{1}{2}}, & \text{if } T < |T_c|, \\ 0, & \text{otherwise,} \end{cases} \qquad \text{(A8)}$$

as can be seen in Fig. 16. The final result interval for the critical temperature is then given by the estimated values for different system sizes. This procedure causes significant errors compared to the previous method and fails to account for finite-size effects that may occur. Nevertheless, the errors are small enough to permit analysis as can be seen in Fig. 11.

APPENDIX B: FINITE-TEMPERATURE PP-DMRG

In order to use time-evolution methods that are designed for long-range interactions, we choose the SYMMPS toolkit [62]. This choice comes with the caveat that conserved U(1) quantum numbers are necessary. Since the MPS $+$ MF Hamiltonian does violate those symmetries, we apply PP-DMRG [60] to restore them. That means we not only double the system size in order to represent density matrices instead
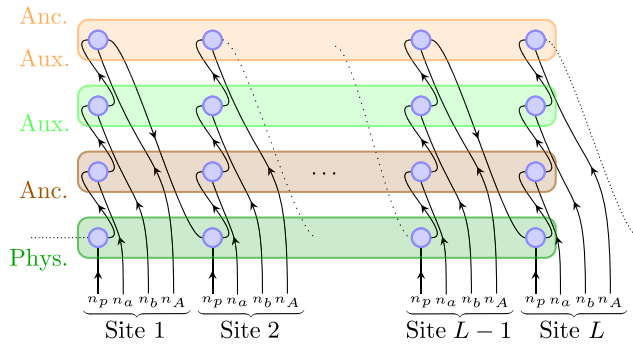
FIG. 17.   Structure of MPS for thermal-state calculations using state purification and imaginary-time evolution via TDVP, which requires introducing ancilla sites. The use of the SYMMPS package [62] for TDVP also requires using PP-DMRG [60], meaning adding auxiliary sites for both physical and ancilla sites to recover conserved charge and spin quantum numbers.

of states, as is usually the case in state purification [66,67], but also double it again in order to have an auxiliary bath to restore the conservation laws via these added bath sites. Hence, as can be seen in Fig. 17, we have the physical and the ancilla system, which represent density matrices, and the auxiliary and the ancilla-auxiliary system, which restore the quantum number conservation.

Since the long-range interactions are thus increased in their range by a factor of 4, another obstacle needs to be circumvented: This is the loss of particles from the physical (and its auxiliary) system into the ancilla (and its auxiliary) system [45]. This leakage occurs due to the accumulation of numerical errors, which we prevent by having the U(1) symmetries conserved on the physical and the ancilla system separately. To achieve that, we increase the local basis from four to 16 states by adding a separate fermionic particle species, which is supposed to occur only on the ancilla systems.

Evolving a product state, such as an infinite-temperature state, with TDVP leads to significant projection errors [45]. Hence, one needs to increase the bond dimension first via a different time-evolution method [12,68]. We choose to use two-site TDVP for the first ten time steps, which are chosen to be very small $\delta t = 10^{-7}$. This way, the bond dimension grows, but the projection error, which is scaled within the exponential by the time step, stays small. Afterward, one time step is performed to go to the usual time step grid $\delta t = 0.05$. Then, all following time steps are executed by single-site TDVP, since that is faster.

APPENDIX C: TRUNCATION ERROR EXTRAPOLATION

For any local quantity, it is possible to perform an extrapolation in the truncation error. For large enough bond dimension, a general measurement follows:

$$\langle O \rangle(\epsilon_\psi) = \langle O \rangle + c_0 \epsilon_\psi; \tag{C1}$$

i.e., a measurement of a DMRG state typically depends linearly on its truncation error [46,69,70].

APPENDIX D: AUXILIARY-FIELD QUANTUM MONTE CARLO

There are a number of different flavors of the AFQMC method, which are documented in the literature [39–42]. In this work, the ground-state order parameters from AFQMC are obtained using a generalized METROPOLIS approach with force bias [63], while the T_{BKT} is obtained with the standard finite-temperature AFQMC method [71,59]. In this appendix, we briefly describe our ground-state and finite-temperature calculations in two separate subsections below.

1. Ground-state order parameter

Here we briefly describe our ground-state AFQMC calculations and how the superconducting order parameters are obtained. A comprehensive discussion of AFQMC can be found in Refs. [40,72].

The ground-state AFQMC method solves the Schrödinger equation of the quantum many-body problem by projecting out the ground-state wave function $|\Psi_G\rangle$ of the system from an initial wave function $|\Psi_I\rangle$:

$$e^{-\beta H}|\Psi_I\rangle \propto |\Psi_\beta\rangle \xrightarrow{\beta \to \infty} |\Psi_G\rangle. \tag{D1}$$

The initial wave function is generally obtained from a mean-field calculation, for example, with the Hartree-Fock method. When the imaginary-time β is sufficiently large, the projected wave function $|\Psi_\beta\rangle$ approaches the ground state $|\Psi_G\rangle$ of H.

Numerically, the propagator $e^{-\beta H}$ is rewritten in a one-body form. This is achieved by first discretizing the imaginary time into small time steps $\Delta\tau$,

$$e^{-\beta H} = (e^{-\Delta\tau H})^m. \tag{D2}$$

In this work, $\Delta\tau$ is set to be 0.01 for the ground-state algorithm. We verify this to give Trotter errors well within our statistical error in the final results. Then we apply a Trotter-Suzuki breakup for each small imaginary step,

$$e^{-\Delta\tau H} = e^{-\Delta\tau K/2}e^{-\Delta\tau V}e^{-\Delta\tau K/2} + \mathcal{O}(\Delta\tau^3), \tag{D3}$$

where K is the kinetic part of the Hamiltonian containing only one-body terms, while V is the potential part, which consists of two-body terms.

To rewrite all two-body terms into one-body terms, we apply the Hubbard-Stratonovich transformation in a charge decomposition form:

$$e^{-\Delta\tau U n_{i,\uparrow} n_{i,\downarrow}} = \frac{1}{2} \sum_{x_i=\pm 1} e^{(\gamma x_i - \Delta\tau U/2)(n_{i,\uparrow}+n_{i,\downarrow}-1)}$$

$$\equiv \frac{1}{2} \sum_{x_i=\pm 1} b_i(x_i), \tag{D4}$$

where $\cosh(\gamma) = \exp(-\Delta\tau U/2)$. With the above transformation, the short-time propagator can be written as

$$e^{-\Delta\tau H} = \int d\mathbf{x}\, p(\mathbf{x}) B(\mathbf{x}), \tag{D5}$$

where $B(\mathbf{x}) = e^{-\Delta\tau K/2} \prod_i b_i(x_i) e^{-\Delta\tau K/2}$ is now a one-body propagator, and $p(\mathbf{x})$ is a probability density function, which in the form above is uniform in the AF configurations $\mathbf{x} = \{x_1, x_2, ..., x_{N_l}\}$.

Ground-state observables are given by

$$\langle O \rangle = \frac{\langle \Psi_L | O | \Psi_R \rangle}{\langle \Psi_L | \Psi_R \rangle}, \tag{D6}$$

where $\langle \Psi_L | = \langle \Psi_I | e^{-\beta_L H}$ and $|\Psi_R\rangle = e^{-\beta_R H}|\Psi_I\rangle$. In our calculations with the generalized METROPOLIS algorithm, we choose a total projection time β, which defines a fixed length of the imaginary-time path integral. The location along the path where O is measured moves with our sampling; for example, as we sweep from left to right, we start measuring when $\beta_L > \beta_{\rm eq}$, where $\beta_{\rm eq} < \beta/2$ is a parameter which ensures that the asymptotic limit in Eq. (D1) is reached (in a numerical sense), and $\beta_R \equiv \beta - \beta_L$. Conversely, when we sweep from right to left, the measurement starts when $\beta_R > \beta_{\rm eq}$ and stops when $\beta_L \equiv \beta - \beta_R$ reaches $\beta_{\rm eq}$. The expectation $\langle O \rangle$ is expressed as path integrals in AF space:

$$\langle O \rangle = \frac{\int \frac{\langle \phi_L | O | \phi_R \rangle}{\langle \phi_L | \phi_R \rangle} P(X) \langle \phi_L | \phi_R \rangle dX}{\int P(X) \langle \phi_L | \phi_R \rangle dX}. \tag{D7}$$

In Eq. (D7), $X \equiv \{\mathbf{x}^{(M)}, \mathbf{x}^{(M-1)}, ..., \mathbf{x}^{(2)}, \mathbf{x}^{(1)}\}$, which is an MN_l-dimensional vector, denotes the AF configuration of the entire path, with $M \equiv \beta/\Delta\tau$ being the number of time slices in the path, and the probability function $P(X) = \prod_{m=1}^{M} p(\mathbf{x}^{(m)})$. The wave functions $|\phi_R\rangle$ and $|\phi_L\rangle$ are single Slater determinants (if we choose $|\Psi_I\rangle$ to be a single Slater determinant), and have the form $|\phi_R\rangle = \prod_{m=1}^{M_R} B(\mathbf{x}^{(m)})|\Psi_I\rangle$ and, correspondingly, $\langle \phi_L | = \langle \Psi_I | \prod_{m=1}^{M_L} B(\mathbf{x}^{(M-m+1)})$, with $M_R \equiv \beta_R/\Delta\tau$ and $M_L \equiv \beta_L/\Delta\tau$. A heat-bath-like algorithm and a cluster update scheme are incorporated in our generalized METROPOLIS algorithm, which is described in detail in Appendix A of Ref. [63].

The pair correlator (the pair-pair correlation) can be computed by the path integral above in Eq. (D7). For each path, if we denote the expectation value $\langle \phi_L | O | \phi_R \rangle / \langle \phi_L | \phi_R \rangle$ by $\langle O \rangle_{L,R}$, then $\langle c_{i,\uparrow}^\dagger c_{i,\downarrow}^\dagger c_{j,\downarrow} c_{j,\uparrow} \rangle_{L,R}$ can be
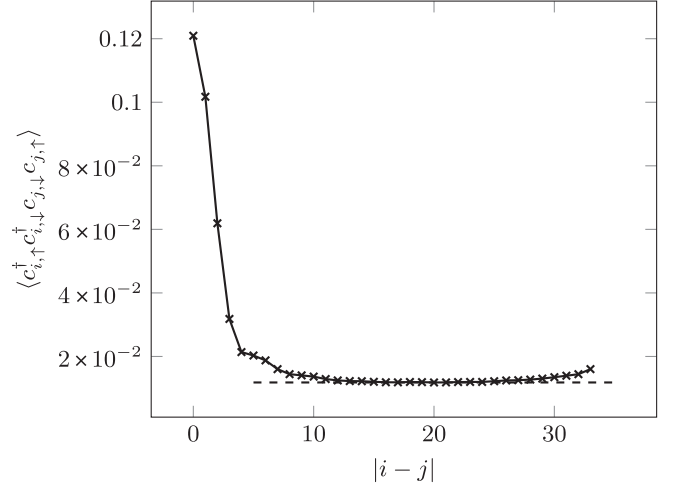

FIG. 18. Example of on-chain pair correlator in ground-state AFQMC for a 40×4 lattice with $U = -2t$, $t_\perp \approx 0.14t$, $n = 0.5$. We extract the effective order parameter for superconductivity from the square root of the long-distance behavior (dashed line).

decomposed by Wick's theorem into pair products of one-body Green's functions:

$$\langle c_{j,\sigma}^\dagger c_{i,\sigma} \rangle_{L,R} \equiv \frac{\langle \phi_L | c_{j,\sigma}^\dagger c_{i,\sigma} | \phi_R \rangle}{\langle \phi_L | \phi_R \rangle}$$

$$= [\Phi_R^\sigma [(\Phi_L^\sigma)^\dagger \Phi_R^\sigma]^{-1} (\Phi_L^\sigma)^\dagger]_{i,j}, \tag{D8}$$

where Φ_L and Φ_R are the matrix representation of the kets $|\phi_L\rangle$ and $|\phi_R\rangle$, respectively.

We choose a reference site and then compute the pair correlator between the reference site and other different lattice sites, as shown in Fig. 18. We then average the pair correlation of the sites that have the longest distance. To further reduce statistical error, the reference point is averaged over the whole lattice, since each lattice site is equivalent under periodic boundary condition.

2. Kosterlitz-Thouless transition temperature

For finite-temperature results we use ALF. The structure of the algorithm is similar to that of ground-state AFQMC previously outlined, and we refer the reader to the ALF documentation [41,42].

Using ALF we obtain results for any value of imaginary-time β. From linear response theory, it is possible to relate the superfluid weight to current-current correlators and kinetic energy [59,71]:

$$\frac{D_s}{4\pi e^2} = \frac{1}{4}[\langle -k_x \rangle - \Lambda_{xx}(q_x = 0, q_y \to 0, i\omega_m = 0)], \tag{D9}$$

$$0 = \langle -k_x \rangle - \Lambda_{xx}(q_x \to 0, q_y = 0, i\omega_m = 0). \tag{D10}$$

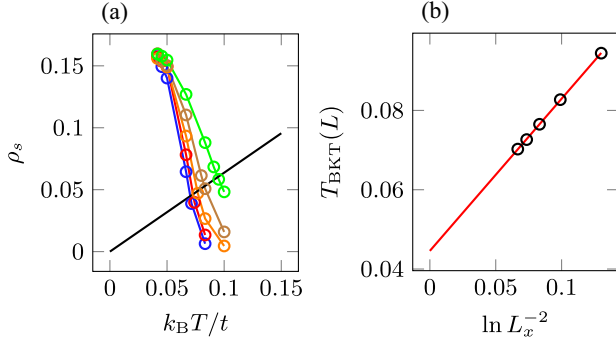For the KT transition, we expect that [73]

FIG. 19. Strategy for obtaining T_{BKT} for the parameters $U = -4t$, $t_\perp \approx 0.28t$, and $\mu = -0.6533t$. In (a) an intersection of ρ_s and $2T/\pi$ indicating $T_{\mathrm{BKT}}(L)$, and (b) the thermodynamic limit of T_{BKT} obtained through Eq. (D13). The aspect ratio is chosen such that $L_y = L_x/4$.

$$\lim_{T \to T_{\mathrm{BKT}}} \frac{T}{\rho_s} = \frac{\pi}{2}, \tag{D11}$$

where $\rho_s = (D_s/4\pi e^2)$ is the helicity modulus. Thus, the straight line in $\rho_s - T$ space,

$$\rho_s = \frac{2T}{\pi}, \tag{D12}$$

intersects at $T = T_{\mathrm{BKT}}$. An example of this is shown in Fig. 19(a).

This calculation is performed for each size of the system, yielding a trend of the finite-size T_{BKT} which is then extrapolated to the thermodynamic limit using the form [74]

$$T_{\mathrm{BKT}}(L) = T_{\mathrm{BKT}} + \frac{A}{\ln L^2}. \tag{D13}$$

An example of this fit is shown in Fig. 19(b).

3. Density

The AFQMC finite-temperature algorithm from the ALF Collaboration uses the Blankenbecler-Scalapino-Sugar algorithm [41,42,75]. This algorithm works in the grand canonical ensemble as is necessary and will not have fixed density. In general, we are interested in specifying the
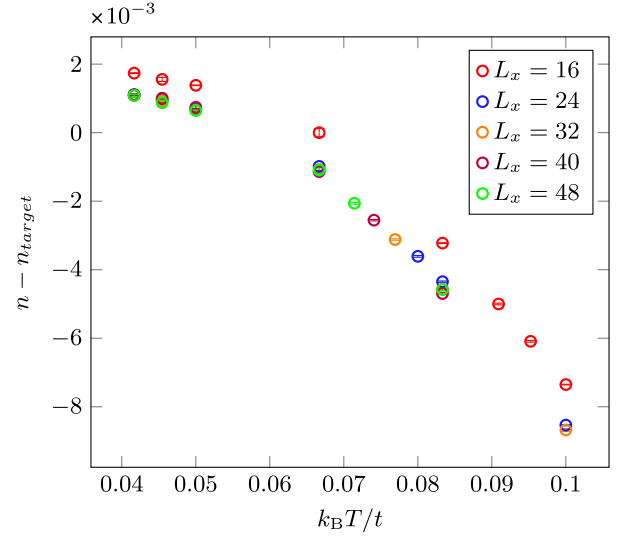

FIG. 20. The density over temperature for a given chemical potential $\mu = -0.6533t$ at parameters $U = -4t$ and $t_\perp \approx 0.28t$. The aspect ratio is chosen such that $L_y = L_x/4$.

density to work at as T_{BKT} will have some dependence on this quantity.

Precisely fixing the density requires simulation of a large number of chemical potential values. In order to alleviate this problem, we run simulations for a small number of lattice points and determine the correct chemical potential for a given temperature. We then use this value of chemical potential for all lattice sizes and temperatures of that parameter set. This will yield a notable error in density as shown in Fig. 20. At the same time, we find that T_{BKT} is only modestly affected by density.

APPENDIX E: ARRAY OF HUBBARD LADDERS

We derive the effective 1D model for the weakly coupled Hubbard ladders starting from the 3D array given by

$$H_{\mathrm{3D}} = \sum_{k,l} H_{\mathrm{HL}}(\mathbf{R}_{k,l}) + t_\perp H_\perp, \tag{E1}$$

where

$$H_{\mathrm{HL}}(\mathbf{R}_{k,l}) = -t \sum_{i=1}^{L-1} \sum_{j=0}^{1} \sum_\sigma (c_{i+1,j,\sigma}^\dagger(\mathbf{R}_{k,l}) c_{i,j,\sigma}(\mathbf{R}_{k,l}) + c_{i,j,\sigma}^\dagger(\mathbf{R}_{k,l}) c_{i+1,j,\sigma}(\mathbf{R}_{k,l})) - \mu \sum_{i,j} n_{i,j}(\mathbf{R}_{k,l})$$

$$- t' \sum_{i=1}^{L} \sum_\sigma (c_{i,1,\sigma}^\dagger(\mathbf{R}_{k,l}) c_{i,0,\sigma}(\mathbf{R}_{k,l}) + c_{i,0,\sigma}^\dagger(\mathbf{R}_{k,l}) c_{i,1,\sigma}(\mathbf{R}_{k,l})) + U \sum_{i,j} n_{i,j,\uparrow}(\mathbf{R}_{k,l}) n_{i,j,\downarrow}(\mathbf{R}_{k,l}).$$

The vector $\mathbf{R}_{k,l}$ denotes the position of the ladder in a 2D grid. We use the definition ($\mathbf{R}_{k,l}$ suppressed)

$$n_{i,j} = \sum_\sigma c_{i,j,\sigma}^\dagger c_{i,j,\sigma} = \sum_\sigma n_{i,j,\sigma}, \tag{E2}$$

and $c_{i,j,\sigma}$ follow the usual anticommutation relations.

So far, we have described only a set of Fermi-Hubbard ladders. The added Hamiltonian $H_\perp$ is defined by

$$H_\perp = -\sum_{i,l}^{L} \sum_{k=1}^{L-1} \sum_\sigma [c_{i,1,\sigma}^\dagger(\mathbf{R}_{k,l})c_{i,0,\sigma}(\mathbf{R}_{k+1,l}) + c_{i,0,\sigma}^\dagger(\mathbf{R}_{k+1,l})c_{i,1,\sigma}(\mathbf{R}_{k,l})]$$

$$-\sum_{i,k}^{L} \sum_j \sum_{l=1}^{L-1} \sum_\sigma [c_{i,j,\sigma}^\dagger(\mathbf{R}_{k,l})c_{i,j,\sigma}(\mathbf{R}_{k,l+1}) + c_{i,j,\sigma}^\dagger(\mathbf{R}_{k,l+1})c_{i,j,\sigma}(\mathbf{R}_{k,l})]. \tag{E3}$$

Note that movement to neighboring ladders may change what leg one is on. This is due to half of neighboring ladders being side-by-side neighbors and the other half being front-and-back neighbors.

1. Effective Hubbard-ladder Hamiltonian

When U is strongly repulsive and density is close to unit filling, H_{HL} and thus also the full set of ladders have a spectrum which contains clusters of energy eigenstates separated by large gaps. Thus, analogous to Eq. (9) it is possible to derive an effective Hamiltonian

$$H_{3D}^{\mathrm{eff}} = \sum_{k,l} H_{\mathrm{HL}}(\mathbf{R}_{k,l}) - \frac{t_\perp^2}{\Delta E_p} P_0 H_\perp^2 P_0, \tag{E4}$$

where

$$\Delta E_p = 2E(N+1, 1/2) - E(N, 0) - E(N+2, 0) \tag{E5}$$

is the pairing energy for a single ladder at particle number N, and $E(N, S)$ is the energy of a ladder at particle number N and spin S. The operator P_0 is a projector to the lowest-energy manifold of the total system. As in Sec. II A, this removes certain terms within $H_\perp^2$, such as two particles moving to two separate ladders.

Expanding $P_0 H_\perp^2 P_0$ yields a new operator which is quartic and acts like an effective interaction. Each interaction involves particles on two different ladders, e.g., moving two particles from one ladder to an adjacent one.

2. Mean-field Hamiltonian

With a quartic interaction where half the operators involve one ladder and the other half involve the other, we can make an ansatz of quasifree states:

$$\langle c_i^\dagger c_j^\dagger c_k c_l \rangle = \langle c_i^\dagger c_j^\dagger \rangle \langle c_k c_l \rangle + \langle c_i^\dagger c_l \rangle \langle c_j^\dagger c_k \rangle - \langle c_i^\dagger c_k \rangle \langle c_j^\dagger c_l \rangle. \tag{E6}$$

This allows us to create a mean-field Hamiltonian which produces expectation values of this form. In the process, we assume that expectation values involving operators on different ladders are of negligible size and ignore them. This leads to the mean-field Hamiltonian (for one ladder)

$$H_{\mathrm{MF}} = H_{\mathrm{HL}} - H_{\mathrm{pair}} - H_{\mathrm{exc}}, \tag{E7}$$

where

$$H_{\mathrm{pair}} = \sum_{i,i',j,j'} \alpha_{i,i',j,j'} (c_{i,j,\downarrow}^\dagger c_{i',j',\uparrow}^\dagger + c_{i',j',\uparrow} c_{i,j,\downarrow}), \tag{E8}$$

$$H_{\mathrm{exc}} = -\sum_{i,i',j,j',\sigma} \beta_{i,i',j,j',\sigma} c_{i,j,\sigma}^\dagger c_{i',j',\sigma}, \tag{E9}$$

and the pairing amplitudes are given by

$$\alpha_{i,i',0,0} = \frac{2t_\perp^2}{E_p} (\langle c_{i',1,\uparrow} c_{i,1,\downarrow} \rangle + 2\langle c_{i',0,\uparrow} c_{i,0,\downarrow} \rangle), \tag{E10}$$

$$\alpha_{i,i',1,1} = \frac{2t_\perp^2}{E_p} (\langle c_{i',0,\uparrow} c_{i,0,\downarrow} \rangle + 2\langle c_{i',1,\uparrow} c_{i,1,\downarrow} \rangle), \tag{E11}$$

$$\alpha_{i,i',1,0} = \frac{4t_\perp^2}{\Delta E_p} \langle c_{i',0,\uparrow} c_{i,1,\downarrow} \rangle, \tag{E12}$$

$$\alpha_{i,i',0,1} = \frac{4t_\perp^2}{\Delta E_p} \langle c_{i',1,\uparrow} c_{i,0,\downarrow} \rangle, \tag{E13}$$

whereas the exchange terms are given by

$$\beta_{i,i',0,0,\sigma} = \frac{2t_\perp^2}{E_p} (\langle c_{i,1,\sigma}^\dagger c_{i',1,\sigma} \rangle + 2\langle c_{i,0,\sigma}^\dagger c_{i',0,\sigma} \rangle), \tag{E14}$$

$$\beta_{i,i',1,1,\sigma} = \frac{2t_\perp^2}{E_p}(\langle c_{i,0,\sigma}^\dagger c_{i',0,\sigma}\rangle + 2\langle c_{i,1,\sigma}^\dagger c_{i',1,\sigma}\rangle), \quad (E15)$$

$$\beta_{i,i',1,0,\sigma} = \frac{4t_\perp^2}{E_p}\langle c_{i',0,\sigma}^\dagger c_{i,1,\sigma}\rangle, \quad (E16)$$

$$\beta_{i,i',0,1,\sigma} = \frac{4t_\perp^2}{E_p}\langle c_{i',1,\sigma}^\dagger c_{i,0,\sigma}\rangle. \quad (E17)$$

Note that the Hermiticity of Eq. (E9) is not apparent from the expression but is hidden in the sum.

APPENDIX F: ANALYTICAL T_c AND GAP $\Delta_\rho(T=0)$

Here we give details on how to explicitly compute the value of the ratio between T_c and the charge gap $\Delta_\rho(T=0)$ when there is only one massless sector. For T_c, we study how the mean-field order parameter approaches zero above the critical temperature $T > T_c$. For the gap, the effective Hamiltonian is sine-Gordon-like, and its spectrum is largely studied in the literature. We thus rely on the exact solution of the gap and the perturbative one of T_c.

The critical temperature can be estimated by noticing that close to $T \sim T_c$ the order parameter approaches zero. As stated in Ref. [48], we can expand the right-hand side of the self-consistent condition Eq. (38) in powers of the (real) order parameter itself $\Psi_c = \langle \Psi^\dagger \rangle = \langle \psi_\uparrow^\dagger(x)\psi_\downarrow^\dagger(x)\rangle$. In the path-integral formalism, the expansion in power of $\Psi_c(T \simeq T_c) \ll 1$ of the average reads

$$\Psi_c = \frac{1}{\mathcal{Z}_{\theta_\rho}}\int \mathcal{D}\theta_\rho e^{-\mathcal{S}_{\theta_\rho}^{(0)} + \bar{t}_\perp \Psi_c \int d\mathbf{r}(\Psi(\mathbf{r}) + \Psi^\dagger(\mathbf{r}))}\Psi(\mathbf{r}')$$

$$\simeq \frac{\int \mathcal{D}\theta_\rho e^{-\mathcal{S}_{\theta_\rho}^{(0)}} e^{\bar{t}_\perp \Psi_c \int d\mathbf{r}(\Psi(\mathbf{r}) + \Psi^\dagger(\mathbf{r}))}\Psi(\mathbf{r}')}{\mathcal{Z}_{\theta_\rho}^{(0)}(1 + \mathcal{O}(\Psi_c))}$$

$$\simeq \langle e^{\bar{t}_\perp \Psi_c \int d\mathbf{r}(\Psi(\mathbf{r}) + \Psi^\dagger(\mathbf{r}))}\Psi(\mathbf{r}')\rangle_0$$

$$= \bar{t}_\perp \Psi_c \int d\mathbf{r}\langle \Psi^\dagger(\mathbf{r})\Psi(0,0)\rangle_0 + \mathcal{O}(\Psi_c^2), \quad (F1)$$

where the integration over $\mathcal{D}\theta_\rho$ stands for averaging over all possible configurations and $\mathbf{r} = (x,\tau)$, which means that $\int d\mathbf{r} = \int_0^L dx \int_0^\beta d\tau$, with τ the imaginary time. The letter $\mathcal{S}$ denotes the action and $\mathcal{Z}$ the partition function, while the superscript "0" refers to the quadratic component of the mean-field Hamiltonian. The effective coupling is $\bar{t}_\perp = (t_\perp^2/\Delta_\sigma)z_c$. If we neglect second-order terms, the resulting equation reads

$$1 + \bar{t}_\perp g_1^R(k = \omega = 0, T \simeq T_c) = 0, \quad (F2)$$

with g_1^R being the zero component Fourier transform of the retarded correlation function. It is defined as

$$g_1^R(\mathbf{r}, T) = -\langle \mathcal{T}_\tau \Psi(\mathbf{r})\Psi^\dagger(0,0)\rangle_0$$

$$= -(A_F\rho_0 C)^2\langle \mathcal{T}_\tau e^{i\sqrt{2}\theta_\rho(\mathbf{r})} e^{-i\sqrt{2}\theta_\rho(0)}\rangle_0$$

$$= -(A_F\rho_0 C)^2 e^{-\langle [\theta_\rho(\mathbf{r}) - \theta(0)]^2\rangle_0}, \quad (F3)$$

where we write explicitly the imaginary-time (τ) ordering operator $\mathcal{T}_\tau$. In the thermodynamical limit, such averages $\langle\ldots\rangle_0$ are well-known quantities and can be exactly computed in 1D systems for quadratic Hamiltonians [4]. By analytically continuing to real time $\tau = it + \epsilon(t)$, with $\epsilon(t) = \text{sgn}(t)\epsilon$, the critical temperature is

$$T_c = \left[\frac{t_\perp^2}{2\Delta_\sigma}C^2 z_c \frac{(\rho_0 A_F)^2}{u_\rho}\sin\left(\frac{\pi}{2K_\rho}\right)\left(\frac{2\pi\alpha}{u_\rho}\right)^{\frac{1}{K_\rho}}\left(\frac{u_\rho}{2\pi}\right)^2 B^2\left(\frac{1}{4K_\rho}, 1 - \frac{1}{2K_\rho}\right)\right]^{\frac{K_\rho}{2K_\rho - 1}}, \quad (F4)$$

with $B(x,y) = \Gamma(x)\Gamma(y)/\Gamma(x+y)$ the beta function and A_F a prefactor that depends on the specific microscopic model. The choice of the cutoff α is arbitrary but should be sufficiently small so that the spectrum can be linearized. Moreover, the nonuniversal constant A_F is such that the final result is cutoff independent.

The charge gap is instead computed by noticing that the effective model is expressed by a sine-Gordon Hamiltonian. By using the variational method, thus, approximating $\cos\theta \sim 1 - \frac{1}{2}\theta^2$ and computing the action [4], we have that the spectrum is gapped and behaves as $E(k) = \sqrt{(uk)^2 + \Delta_{\text{var}}^2}$. Even if the variational method gives the right scaling for the gap $\Delta_\rho(t_\perp)$, here we use the exact formula [53] so we have also the exact prefactors

$$\Delta_\rho(T = 0) = u_\rho\left[(\rho_0 A_F)^2\alpha^{\frac{1}{K_\rho}}\frac{K_\rho/2}{\kappa^2(K_\rho/2)(4K_\rho - 1)}\tan\left(\frac{\pi}{2}\frac{1}{4K_\rho - 1}\right)\frac{z_c}{u_\rho}\frac{t_\perp^2 C^2}{2\Delta_\sigma}\right]^{\frac{K_\rho}{2K_\rho - 1}}\sin\left(\frac{\pi}{4K_\rho - 1}\right), \quad (F5)$$

with $\kappa(K)$ a combination of gamma functions $\Gamma(K)$,

$$\kappa(K) = \frac{1}{2\sqrt{\pi}} \frac{\Gamma(\frac{1}{8K})\Gamma(\frac{1}{2}\frac{8K}{8K-1})}{\Gamma(1-\frac{1}{8K})\Gamma(\frac{1}{2}\frac{1}{8K-1})}. \tag{F6}$$

Notably, the unknown constants cancel out if we consider the ratio Eq. (40). Moreover, this value depends only on the interaction U, which modifies the Luttinger parameter K_ρ. We recall that this result is valid as long as $t_\perp$ is the smallest energy scale of the problem.

APPENDIX G: RENORMALIZATION-GROUP THEORY

In this section, we give details on the RG procedure implemented to describe an effective 1D Hubbard chain when interactions are small and the pair size is much larger than the microscopic cutoff ("lattice spacing"). The idea is to integrate out all degrees of freedom corresponding to energies between the bandwidth W (corresponding to microscopic cutoff α_0) and the spin gap Δ_σ (corresponding to the pair size $\xi_\sigma = u_\sigma/\Delta_\sigma$). It is important to underline that the RG treatment is only valid when $\Delta_\sigma < W$.

1. First step RG: Renormalization of charge and spins

In order to find the RG equations, we compute perturbatively (in the couplings) the correlation $\langle \psi^\dagger(x)\psi(x) \rangle$ [4,76]. Let us start from the Luttinger parameter K_σ and the dimensionless interaction $g = (U/\pi v_F)$, with v_F the Fermi velocity

$$\frac{dK_\sigma(l)}{dl} = -\frac{K_\sigma^2(l)g^2(l)}{2},$$
$$\frac{dg(l)}{dl} = [2 - 2K_\sigma(l)]g(l). \tag{G1}$$

Because the system is spin isotropic, the equations are equivalent to the ones from the XY problem [77]. For $U < 0$, we flow toward larger g and smaller K_σ, and we need to stop the flow when $g \propto \mathcal{O}(1)$, say, at the RG length l_1. This fictitious length is defined from $\alpha(l) = \alpha(l=0)e^l$ with $\alpha(l=0)$ the original cutoff (lattice spacing).

In the presence of interchain tunneling, we need to complete the above equations by the ones generated by the interchain tunneling:

$$\frac{dt_\perp(l)}{dl} = \left(2 - \frac{\tilde{K}_\rho + \tilde{K}_\sigma(l)}{4}\right)t_\perp(l),$$
$$\frac{d\tilde{J}(l)}{dl} = \left(2 - \frac{1}{K_\rho} - K_\sigma(l)\right)\tilde{J}(l) + \tilde{J}_s(l), \tag{G2}$$

where $\tilde{K}_\nu = K_\nu + K_\nu^{-1}$. The dimensionless couplings are defined as

$$\tilde{J} = \frac{\pi\alpha^2}{4u_\rho}(\rho_0 A_F)^2 J \quad \text{and} \quad \tilde{J}_s = \frac{\alpha^2}{2u_\rho^2}t_\perp^2, \tag{G3}$$

and the subscript s stands for source term. Note that the transverse hopping is also, in principle, contributing to the renormalization of the other parameters Eq. (G1) and of K_ρ. In practice, because we consider that the interchain tunneling is the smallest quantity in the problem and in particular that $t_\perp \ll \Delta_\sigma$, we neglect such a renormalization in the first step of the RG. In particular K_ρ can be considered as essentially constant in the first step of the RG. Note also that the combination of interchain hopping and interactions lead to a modification of the naive scaling of the interchain tunneling. In addition to its own renormalization, the single-particle interchain tunneling also generates via RG the pair tunneling. This is due to the fact that pairs of electrons that hop within a distance $|r_1 - r_2| < \alpha(l)$ are to be considered local. Moreover, we need to enforce the condition $\tilde{J}(l=0) = 0$ because the original Hamiltonian Eq. (1) has only single-particle hopping, not pair hopping. It is clear that, as we renormalize, the pair-hopping term is generated and eventually will be the relevant coupling. It easy to see that if from Eq. (G1) we flow toward smaller K_σ, then the $1/K_\sigma$ term in Eq. (G2) makes $t_\perp$ an irrelevant coupling.

We have to stop this first step of the flow when the coupling constant in Eq. (G1) is of order one. At that scale ($l = l_1$), the microscopic cutoff is of the order of the pair size. Another estimation of l_1 is the pair size $\alpha(l_1) \sim u_\sigma/\Delta_\sigma$ where Δ_σ is the spin gap and u_σ is the velocity of the spin sector, before pairs become local. At that scale, the single-particle tunneling is suppressed because of the gap in the spin sector which can be formally seen in the RG equations, Eq. (G2), by the fact that for small K_σ, $t_\perp$ is formally irrelevant.

2. Second RG step: Pair hopping and dimensional crossover

In the second RG step $l > l_1$, we have only pair hopping, and spin excitations and single-particle hopping are suppressed. The spin sector is out of the picture, and the RG equation expressing the pair-hopping coupling becomes

$$\frac{d\tilde{J}(l)}{dl} = \left(2 - \frac{1}{K_\rho}\right)\tilde{J}(l). \tag{G4}$$

We thus see that at the scale l_1 we are now left with only the charge sector as a massless sector and an effective Josephson coupling between the chains. The situation is thus similar to the one we had in the large spin-gap limit but with a different Josephson coupling than the strong-coupling limit $J \sim (t_\perp^2/\Delta_\sigma)$. This has consequences for the absolute values of the T_c and charge gap at zero temperature but the ratio is unchanged compared to Eq. (40).

The absolute values of the T_c or the charge gap can simply be computed by continuing the flow of Eq. (G4) until the Josephson coupling itself becomes of order one.

The scale at which the Josephson coupling reaches this magnitude defines a second RG length l^*. The condition is set by $\tilde{J}(l^*) \propto \mathcal{O}(1)$, which means that for $l > l^*$ the coupling is so large that we are back to a 2D or 3D system. From this length, we can define either the critical temperature or the charge gap, because their ratio is fixed from Eq. (40). By integrating Eq. (G4), we find that the RG length l^* at which the dimensional crossover occurs is

$$\alpha(l^*) = \alpha(l_1)\left(\frac{1}{\tilde{J}(l_1)}\right)^{\frac{1}{2-1/K_\rho}}, \tag{G5}$$

with $\alpha(l_1)$ the pair size. Moreover, from dimensional analysis we know that energies scale as $\tilde{\Delta}_\rho(0) = \tilde{\Delta}_\rho(l)e^{-l}$. We observe that $\tilde{\Delta}_\rho(l^*) \propto \tilde{J}(l^*) \sim 1$, and we find that the original (dimensionless) charge gap $\tilde{\Delta}_\rho(0)$ reads

$$\tilde{\Delta}_\rho(0) = \tilde{J}(l_1)^{\frac{1}{2-1/K_\rho}}\frac{\Delta_\sigma}{u_\sigma}\frac{v_F}{W}, \tag{G6}$$

where we define the lattice spacing from $\alpha(l=0) = v_F/W$, the bandwidth as $W = 2t$, and the Fermi velocity $v_F = 2t\sin(\pi\rho_0/2)$, with ρ_0 the unperturbed density (1 at half filling).

Finally, let us note that if we look directly at the pair operator, we have

$$\psi^\dagger_{R,\uparrow}\psi^\dagger_{L,\downarrow} \propto e^{i\sqrt{2}\theta_\rho}\cos(\sqrt{8}\phi_\sigma). \tag{G7}$$

Averaging over the massive spin sector will lead to

$$\psi^\dagger_{R,\uparrow}\psi^\dagger_{L,\downarrow} \propto Ce^{i\sqrt{2}\theta_\rho}, \tag{G8}$$

where the prefactor C could be related to

$$C \propto \langle\cos(\sqrt{8}\phi_\sigma)\rangle_{H_\sigma}. \tag{G9}$$

Because of the gap in the spin sector, this average is nonzero.

---

[1] P. W. Anderson, *The Theory of Superconductivity in the High-Tc Cuprate Superconductors* (Princeton University Press, Princeton, NJ, 1997).

[2] J. Orenstein, *Advances in the Physics of High-Temperature Superconductivity*, Science **288**, 468 (2000).

[3] G. R. Stewart, *Unconventional Superconductivity*, Adv. Phys. **66**, 75 (2017).

[4] T. Giamarchi, *Quantum Physics in One Dimension*, 1st ed. (Oxford University Press, New York, 2003).

[5] G. Karakonstantakis, E. Berg, S. R. White, and S. A. Kivelson, *Enhanced Pairing in the Checkerboard Hubbard Ladder*, Phys. Rev. B **83**, 054508 (2011).

[6] M. Dolfi, B. Bauer, S. Keller, and M. Troyer, *Pair Correlations in Doped Hubbard Ladders*, Phys. Rev. B **92**, 195139 (2015).

[7] F. H. L. Essler and A. M. Tsvelik, *Weakly Coupled One-Dimensional Mott Insulators*, Phys. Rev. B **65**, 115117 (2002).

[8] D. J. Scalapino, *A Common Thread: The Pairing Interaction for Unconventional Superconductors*, Rev. Mod. Phys. **84**, 1383 (2012).

[9] J. P. F. LeBlanc *et al.*, *Solutions of the Two-Dimensional Hubbard Model: Benchmarks and Results from a Wide Range of Numerical Algorithms*, Phys. Rev. X **5**, 041041 (2015).

[10] B.-X. Zheng, C.-M. Chung, P. Corboz, G. Ehlers, M.-P. Qin, R. M. Noack, H. Shi, S. R. White, S. Zhang, and G. K.-L. Chan, *Stripe Order in the Underdoped Region of the Two-Dimensional Hubbard Model*, Science **358**, 1155 (2017).

[11] M. Qin, C. M. Chung, H. Shi, E. Vitali, C. Hubig, U. Schollwöck, S. R. White, and S. Zhang, *Absence of Superconductivity in the Pure Two-Dimensional Hubbard Model*, Phys. Rev. X **10**, 031016 (2020).

[12] A. Wietek, Y. Y. He, S. R. White, A. Georges, and E. M. Stoudenmire, *Stripes, Antiferromagnetism, and the Pseudogap in the Doped Hubbard Model at Finite Temperature*, Phys. Rev. X **11**, 031007 (2021).

[13] A. Bohrdt, C. S. Chiu, G. Ji, M. Xu, D. Greif, M. Greiner, E. Demler, F. Grusdt, and M. Knap, *Classifying Snapshots of the Doped Hubbard Model with Machine Learning*, Nat. Phys. **15**, 921 (2019).

[14] A. Kantian, M. Dolfi, M. Troyer, and T. Giamarchi, *Understanding Repulsively Mediated Superconductivity of Correlated Electrons via Massively Parallel Density Matrix Renormalization Group*, Phys. Rev. B **100**, 075138 (2019).

[15] I. Bloch, J. Dalibard, and W. Zwerger, *Many-Body Physics with Ultracold Gases*, Rev. Mod. Phys. **80**, 885 (2008).

[16] L. W. Cheuk, M. A. Nichols, K. R. Lawrence, M. Okan, H. Zhang, E. Khatami, N. Trivedi, T. Paiva, M. Rigol, and M. W. Zwierlein, *Observation of Spatial Charge and Spin Correlations in the 2D Fermi-Hubbard Model*, Science **353**, 1260 (2016).

[17] M. Boll, T. A. Hilker, G. Salomon, A. Omran, J. Nespolo, L. Pollet, I. Bloch, and C. Gross, *Spin- and Density-Resolved Microscopy of Antiferromagnetic Correlations in Fermi-Hubbard Chains*, Science **353**, 1257 (2016).

[18] M. F. Parsons, A. Mazurenko, C. S. Chiu, G. Ji, D. Greif, and M. Greiner, *Site-Resolved Measurement of the Spin-Correlation Function in the Fermi-Hubbard Model*, Science **353**, 1253 (2016).

[19] A. Mazurenko, C. S. Chiu, G. Ji, M. F. Parsons, M. Kanász-nagy, R. Schmidt, F. Grusdt, E. Demler, D. Greif, and M. Greiner, *A Cold-Atom Fermi-Hubbard Antiferromagnet*, Nature (London) **545**, 462 (2017).

[20] A. Bohrdt, L. Homeier, C. Reinmoser, E. Demler, and F. Grusdt, *Exploration of Doped Quantum Magnets with Ultracold Atoms*, Ann. Phys. (N.Y.) **435**, 168651 (2021).

[21] T. Giamarchi, *Theoretical Framework for Quasi-One Dimensional Systems*, Chem. Rev. **104**, 5037 (2004).

[22] C. Bourbonnais and D. Jérome, *Interacting Electrons in Quasi-One-Dimensional Organic Superconductors*, in *The*

Physics of Organic Superconductors and Conductors, Springer Series in Materials Science Vol. 110, edited by A. Lebed (Springer, Berlin, 2007), p. 358.

[23] A. Bohrdt, L. Homeier, I. Bloch, E. Demler, and F. Grusdt, *Strong Pairing in Mixed Dimensional Bilayer Antiferromagnetic Mott Insulators*, Nat. Phys. **18**, 651 (2022).

[24] S. Hirthe, T. Chalopin, D. Bourgund, P. Bojović, A. Bohrdt, E. Demler, F. Grusdt, I. Bloch, and T. A. Hilker, *Magnetically Mediated Hole Pairing in Fermionic Ladders of Ultracold Atoms*, arXiv:2203.10027.

[25] J.-K. Bao, J.-Y. Liu, C.-W. Ma, Z.-H. Meng, Z.-T. Tang, Y.-L. Sun, H.-F. Zhai, H. Jiang, H. Bai, C.-M. Feng, Z.-A. Xu, and G.-H. Cao, *Superconductivity in Quasi-One-Dimensional $K_2Cr_3As_3$ with Significant Electron Correlations*, Phys. Rev. X **5**, 011013 (2015).

[26] M. D. Watson, Y. Feng, C. W. Nicholson, C. Monney, J. M. Riley, H. Iwasawa, K. Refson, V. Sacksteder, D. T. Adroja, J. Zhao, and M. Hoesch, *Multiband One-Dimensional Electronic Structure and Spectroscopic Signature of Tomonaga-Luttinger Liquid Behavior in $K_2Cr_3As_3$*, Phys. Rev. Lett. **118**, 097002 (2017).

[27] T. Nagata, M. Uehara, J. Goto, J. Akimitsu, N. Motoyama, H. Eisaki, S. Uchida, H. Takahashi, T. Nakanishi, and N. Môri, *Pressure-Induced Dimensional Crossover and Superconductivity in the Hole-Doped Two-Leg Ladder Compound $Sr_{14-x}Ca_xCu_{24}O_{41}$*, Phys. Rev. Lett. **81**, 1090 (1998).

[28] E. Dagotto, *Experiments on Ladders Reveal a Complex Interplay between a Spin-Gapped Normal State and Superconductivity*, Rep. Prog. Phys. **62**, 1525 (1999).

[29] S. Biermann, A. Georges, A. Lichtenstein, and T. Giamarchi, *Deconfinement Transition and Luttinger to Fermi Liquid Crossover in Quasi-One-Dimensional Systems*, Phys. Rev. Lett. **87**, 276405 (2001).

[30] C. Berthod, T. Giamarchi, S. Biermann, and A. Georges, *Breakup of the Fermi Surface near the Mott Transition in Low-Dimensional Systems*, Phys. Rev. Lett. **97**, 136401 (2006).

[31] F. A. Wolf, A. Go, I. P. McCulloch, A. J. Millis, and U. Schollwöck, *Imaginary-Time Matrix Product State Impurity Solver for Dynamical Mean-Field Theory*, Phys. Rev. X **5**, 041032 (2015).

[32] U. Schollwöck, *The Density-Matrix Renormalization Group in the Age of Matrix Product States*, Ann. Phys. (Amsterdam) **326**, 96 (2011).

[33] S. R. White, *Density Matrix Formulation for Quantum Renormalization Groups*, Phys. Rev. Lett. **69**, 2863 (1992).

[34] S. R. White, *Density-Matrix Algorithms for Quantum Renormalization Groups*, Phys. Rev. B **48**, 10345 (1993).

[35] M. Klanjšek, H. Mayaffre, C. Berthier, M. Horvatić, B. Chiari, O. Piovesana, P. Bouillot, C. Kollath, E. Orignac, R. Citro, and T. Giamarchi, *Controlling Luttinger Liquid Physics in Spin Ladders under a Magnetic Field*, Phys. Rev. Lett. **101**, 137207 (2008).

[36] P. Bouillot, C. Kollath, A. M. Läuchli, M. Zvonarev, B. Thielemann, C. Rüegg, E. Orignac, R. Citro, M. Klanjšek, C. Berthier, M. Horvatić, and T. Giamarchi, *Statics and Dynamics of Weakly Coupled Antiferromagnetic Spin-$\frac{1}{2}$ Ladders in a Magnetic Field*, Phys. Rev. B **83**, 054407 (2011).

[37] G. Bollmark, N. Laflorencie, and A. Kantian, *Dimensional Crossover and Phase Transitions in Coupled Chains: Density Matrix Renormalization Group Results*, Phys. Rev. B **102**, 195145 (2020).

[38] E. Stoudenmire and S. R. White, *Studying Two-Dimensional Systems with the Density Matrix Renormalization Group*, Annu. Rev. Condens. Matter Phys. **3**, 111 (2012).

[39] H. Shi and S. Zhang, *Infinite Variance in Fermion Quantum Monte Carlo Calculations*, Phys. Rev. E **93**, 033303 (2016).

[40] S. Zhang, *Many-Body Methods for Real Materials*, edited by E. Pavarini, E. Koch, and S. Zhang (Forschungszentrum Jülich GmbH Institute for Advanced Simulation, Jülich, 2019), Vol. 9.

[41] F. F. Assaad, M. Bercx, F. Goth, A. Götz, J. S. Hofmann, E. Huffman, Z. Liu, F. P. Toldin, J. S. E. Portela, and J. Schwab, *The ALF (Algorithms for Lattice Fermions) Project Release 2.0. Documentation for the Auxiliary-Field Quantum Monte Carlo Code*, SciPost Phys. Codebases (2022) 10.21468/SciPostPhysCodeb.1.

[42] F. F. Assaad, M. Bercx, F. Goth, A. Götz, J. S. Hofmann, E. Huffman, Z. Liu, F. P. Toldin, J. S. E. Portela, and J. Schwab, *Codebase Release 2.0 for ALF (Algorithms for Lattice Fermions)*, SciPost Phys. Codebases (2022) 10.21468/SciPostPhysCodeb.1-r2.0.

[43] S. Martens, G. Bollmark, T. Köhler, S. Manmana, and A. Kantian, *Transient Superconductivity in Three-Dimensional Hubbard Systems by Combining Matrix Product States and Self-Consistent Mean-Field Theory*, arXiv:2207.09841.

[44] C. Cohen-Tannoudji, J. Dupont-Roc, and G. Grynberg, *Transition Amplitudes in Electrodynamics*, in *Atom-Photon Interactions* (John Wiley & Sons, New York, 1998), Chap. 1, pp. 5–66.

[45] S. Paeckel, T. Köhler, A. Swoboda, S. R. Manmana, U. Schollwöck, and C. Hubig, *Time-Evolution Methods for Matrix-Product States*, Ann. Phys. (Amsterdam) **411**, 167998 (2019).

[46] U. Schollwöck, *The Density-Matrix Renormalization Group*, Rev. Mod. Phys. **77**, 259 (2005).

[47] A. F. Ho, M. A. Cazalilla, and T. Giamarchi, *Deconfinement in a 2D Optical Lattice of Coupled 1D Boson Systems*, Phys. Rev. Lett. **92**, 130405 (2004).

[48] M. A. Cazalilla, A. F. Ho, and T. Giamarchi, *Interacting Bose Gases in Quasi-One-Dimensional Optical Lattices*, New J. Phys. **8**, 158 (2006).

[49] N. D. Mermin and H. Wagner, *Absence of Ferromagnetism or Antiferromagnetism in One- or Two-Dimensional Isotropic Heisenberg Models*, Phys. Rev. Lett. **17**, 1133 (1966).

[50] F. D. M. Haldane, *Effective Harmonic-Fluid Approach to Low-Energy Properties of One-Dimensional Quantum Fluids*, Phys. Rev. Lett. **47**, 1840 (1981).

[51] E. H. Lieb and F. Y. Wu, *Absence of Mott Transition in an Exact Solution of the Short-Range, One-Band Model in One Dimension*, Phys. Rev. Lett. **20**, 1445 (1968).

[52] J. R. Schrieffer and P. A. Wolff, *Relation between the Anderson and Kondo Hamiltonians*, Phys. Rev. **149**, 491 (1966).

[53] S. Lukyanov and A. Zamolodchikov, *Exact Expectation Values of Local Fields in the Quantum Sine-Gordon Model*, Nucl. Phys. **B493**, 571 (1997).

[54] F. D. M. Haldane, *General Relation of Correlation Exponents and Spectral Properties of One-Dimensional Fermi Systems: Application to the Anisotropic $S = \frac{1}{2}$ Heisenberg Chain*, Phys. Rev. Lett. **45,** 1358 (1980).

[55] H. J. Schulz, *Correlation Exponents and the Metal-Insulator Transition in the One-Dimensional Hubbard Model*, Phys. Rev. Lett. **64,** 2831 (1990).

[56] T. Giamarchi, *Quantum Physics in One Dimension*, International Series of Monographs on Physics (Oxford University Press, New York, 2004).

[57] T. Giamarchi and B. S. Shastry, *Persistent Currents in a One-Dimensional Ring for a Disordered Hubbard Model*, Phys. Rev. B **51,** 10915 (1995).

[58] A. I. Larkin and J. Sak, *Boundary Conditions for Renormalization-Group Equations in One-Dimensional Fermi Gas*, Phys. Rev. Lett. **39,** 1025 (1977).

[59] T. Paiva, R. R. dos Santos, R. T. Scalettar, and P. J. H. Denteneer, *Critical Temperature for the Two-Dimensional Attractive Hubbard Model*, Phys. Rev. B **69,** 184501 (2004).

[60] T. Köhler, J. Stolpp, and S. Paeckel, *Efficient and Flexible Approach to Simulate Low-Dimensional Quantum Lattice Models with Large Local Hilbert Spaces*, SciPost Phys. **10,** 58 (2021).

[61] I. McCulloch, Matrix Product Toolkit, https://people.smp.uq.edu.au/IanMcCulloch/mptoolkit/index.php (December 1, 2018).

[62] S. Paeckel and T. Köhler, SYMMPS, https://www.symmps.eu (April 1, 2021).

[63] H. Shi, S. Chiesa, and S. Zhang, *Ground-State Properties of Strongly Interacting Fermi Gases in Two Dimensions*, Phys. Rev. A **92,** 033603 (2015).

[64] Y.-Y. He, H. Shi, and S. Zhang, *Reaching the Continuum Limit in Finite-Temperature Ab Initio Field-Theory Computations in Many-Fermion Systems*, Phys. Rev. Lett. **123,** 136402 (2019).

[65] M. Newman and G. Barkema, *Monte Carlo Methods in Statistical Physics* (Oxford University Press, New York, 1999), Vol. 24.

[66] F. Verstraete, J. J. García-Ripoll, and J. I. Cirac, *Matrix Product Density Operators: Simulation of Finite-Temperature and Dissipative Systems*, Phys. Rev. Lett. **93,** 207204 (2004).

[67] A. E. Feiguin and S. R. White, *Finite-Temperature Density Matrix Renormalization Using an Enlarged Hilbert Space*, Phys. Rev. B **72,** 220401(R) (2005).

[68] S. Paeckel, B. Fauseweh, A. Osterkorn, T. Köhler, D. Manske, and S. R. Manmana, *Detecting Superconductivity Out of Equilibrium*, Phys. Rev. B **101,** 180507(R) (2020).

[69] S. R. White and D. A. Huse, *Numerical Renormalization-Group Study of Low-Lying Eigenstates of the Antiferromagnetic $S = 1$ Heisenberg Chain*, Phys. Rev. B **48,** 3844 (1993).

[70] Ö. Legeza and G. Fáth, *Accuracy of the Density-Matrix Renormalization-Group Method*, Phys. Rev. B **53,** 14349 (1996).

[71] D. J. Scalapino, S. R. White, and S. Zhang, *Insulator, Metal, or Superconductor: The Criteria*, Phys. Rev. B **47,** 7995 (1993).

[72] F. F. Assaad, *Quantum Simulations of Complex Many-Body Systems: From Theory to Algorithms*, Publication Series of the John von Neumann Institute for Computing Vol. 10, edited by J. Grotendorst, D. Marx, and A. Muramatsu (NIC, Jülich, 2002), pp. 99–155.

[73] D. R. Nelson and J. M. Kosterlitz, *Universal Jump in the Superfluid Density of Two-Dimensional Superfluids*, Phys. Rev. Lett. **39,** 1201 (1977).

[74] S. T. Bramwell and P. C. W. Holdsworth, *Magnetization and Universal Sub-Critical Behaviour in Two-Dimensional XY Magnets*, J. Phys. Condens. Matter **5,** L53 (1993).

[75] R. Blankenbecler, D. J. Scalapino, and R. L. Sugar, *Monte Carlo Calculations of Coupled Boson-Fermion Systems. I*, Phys. Rev. D **24,** 2278 (1981).

[76] J. V. José, L. P. Kadanoff, S. Kirkpatrick, and D. R. Nelson, *Renormalization, Vortices, and Symmetry-Breaking Perturbations in the Two-Dimensional Planar Model*, Phys. Rev. B **16,** 1217 (1977).

[77] J. M. Kosterlitz, *The Critical Properties of the Two-Dimensional XY Model*, J. Phys. C **7,** 1046 (1974).